Investigation of Microstrip Antenna Arrays of Circular Elements Including Mutual Coupling

by

Kwok-Leung Lawrence Lai

A thesis
presented to the University of Manitoba
in partial fulfillment of the
requirements for the degree of
Master of Science
in
Department of Electrical Engineering

Winnipeg, Manitoba

(c) Kwok-Leung Lawrence Lai, 1987

Permission has been granted to the National Library of Canada to microfilm this thesis and to lend or sell copies of the film.

The author (copyright owner) has reserved other publication rights, and neither the thesis nor extensive extracts from it may be printed or otherwise reproduced without his/her written permission.

L'autorisation a été accordée à la Bibliothèque nationale du Canada de microfilmer cette thèse et de prêter ou de vendre des exemplaires du film.

L'auteur (titulaire du droit d'auteur) se réserve les autres droits de publication; ni la thèse ni de longs extraits de celle-ci ne doivent être imprimés ou autrement reproduits sans son autorisation écrite.

ISBN 0-315-37189-7

INVESTIGATION OF MICROSTRIP ANTENNA ARRAYS OF CIRCULAR ELEMENTS INCLUDING MUTUAL COUPLING

BY

KWOK-LEUNG LAWRENCE LAI

A thesis submitted to the Faculty of Graduate Studies of the University of Manitoba in partial fulfillment of the requirements of the degree of

MASTER OF SCIENCE

© 1987

Permission has been granted to the LIBRARY OF THE UNIVERSITY OF MANITOBA to lend or sell copies of this thesis, to the NATIONAL LIBRARY OF CANADA to microfilm this thesis and to lend or sell copies of the film, and UNIVERSITY MICROFILMS to publish an abstract of this thesis.

The author reserves other publication rights, and neither the thesis nor extensive extracts from it may be printed or otherwise reproduced without the author's written permission.

I hereby declare that I am the sole author of this thesis.

I authorize the University of Manitoba to lend this thesis to other institutions or individuals for the purpose of scholarly research.

Kwok-Leung Lawrence Lai

I further authorize the University of Manitoba to reproduce this thesis by photocopying or by other means, in total or in part, at the request of other institutions or individuals for the purpose of scholarly research.

Kwok-Leung Lawrence Lai

The University of Manitoba requires the signatures of all persons using or photocopying this thesis. Please sign below, and give address and date.

ABSTRACT

A study on how mutual coupling affects the radiation pattern of a microstrip antenna array is presented. The effective voltages and the active input impedance are formulated in terms of the applied voltages and the mutual admittance of the radiating elements. The mutual reaction between circular microstrip radiators is determined using a magnetic current model and the mutual admittance is obtained by applying the reaction concept. A hexagonal array of seven circular microstrips is investigated and the effects on its gain pattern due to the element spacing, the dielectric constant and the thickness of the substrate are determined. A brief study of the multi-layer stacked microstrip antenna and its array shows the structure gives a gain improvement but accompanied with a rapid azimuthal variation.

ACKNOWLEDGEMENTS

The author would like to express his sincere gratitude to Professor L. Shafai for his patience, guidance, and support. To the author, he is more than an adviser. The author would also like to address his deep appreciation to his former advisor, Dr. A. Ittipiboon, for his supervision and all those valuable suggestions. Thankfulness is extended to Dr. A. K. Bhattacharyya for those generous and helpful discussions.

CONTENTS

LIST OF FIGURES

LIST OF TABLES

Chapter I

INTRODUCTION

1.1 HISTORICAL BACKGROUND ON MICROSTRIP ANTENNA

The concept of microstrip antenna was introduced early in the '50s. However, very few research papers or literature were reported regarding to this low profile and conformal antenna in the following two decades. In the early 70's Munson [1] published the development of microstrip antennas for use as low profile flush-mounted antennas on rockets and missiles and their applications in many antenna system problems, and thereby gave birth to a new antenna industry. Additional work on basic microstrip patch element by Howell [2], Derneryd [3], Garvin, Munson, Ostwald, and Schroeder [4], Shen, Long, Allerding, and Walton [5], Agrawal and Bailey [6] were considered to be the backbone on the design and analysis of microstrip antennas.

Basically, microstrip antennas consist of an extremely thin metallic printed strip placed a small fraction of a wavelength ($h \ll \lambda$) above a metallic ground plate. The separation between these two patches is a dielectric substrate. Proper selection of this material depends on its dielectric constant, loss tangent, dimensional stability and tempera-

ture sensitivity. Its thickness variation affects the resonant frequency, resonant resistance, and other antenna quantities. Many different shapes of microstrip patch are present but regular geometric shapes are the most common because of ease of analysis and fabrication. Fig. 1 shows a representative circular microstrip patch and its associated dielectric substrate and ground plane. Feeding is achieved either via a conducting strip to the edge of the patch or through use of a coaxial line with an inner conductor that terminates on the patch. The placement of the feed affects the matching and operation of the antenna. A ground wire is used to connect the center of the disk to the ground plane and forces the electric field to be zero at the point in order to eliminate the excitation of those modes with n=0.

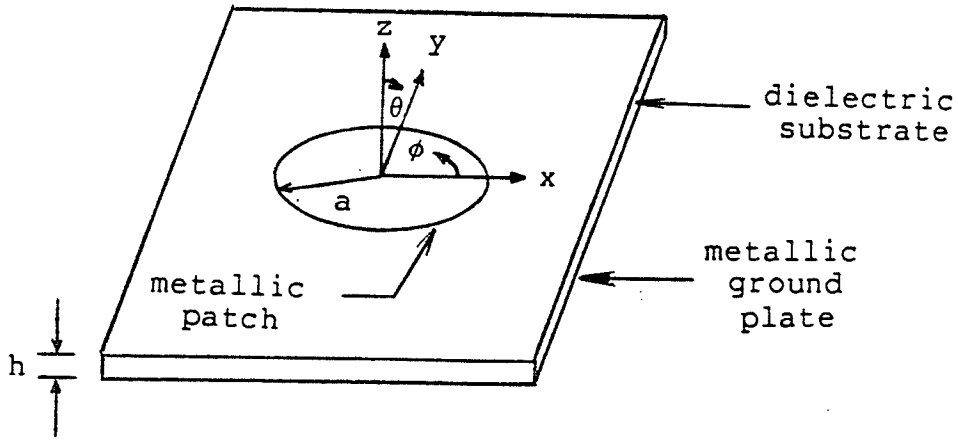

Figure 1: Circular microstrip antenna

In those applications where bandwidths less than a few percent are acceptable, size, weight, cost, performance, ease of installion, and aerodynamic profile are constraints,

microstrip antenna may have the desired characteristics. Either linear or circular polarization can be produced with microstrip antennas. Arrays of microstrip elements, with single or multiple feeds, may also be used to shape the beam, to adjust the beam position, and to obtain greater directivities.

With continuing research and development and increased usage of microstrip antennas, it is expected that they will ultimately replace conventional antennas for most applications including: satellite communication, guided missiles and rockets, remote sensing instrumentation, and biomedical radiator etc.. As awareness of the possibilities of microstrip antennas increases, the number of applications will continue to grow.

1.2 MICROSTRIP ANALYSIS AND ITS RECENT DEVELOPMENT

Early literature reported by Munson [1] on the use of microstrip antenna to achieve an omnidirectional pattern for missiles and satellites has indeed triggered the antenna technology and stimulated researchers for further pursuit on the topic. Prior to Munson, Watkins [7] predicted the resonant frequency of a circular microstrip disk by assuming the patch element as a cylindrical cavity. Theoretical expressions and experimental data on impedance and resonant frequency of circular microstrip disk have been published by Itoh and Mittra [8], Wolff and Knoppik [9], Shen et al.

[5,10], Lo et al. [13], and Chew and Kong [15]. Radiation conductance, antenna efficiency, and other antenna quantities have also been discussed by Derneryd [12]. Most of this valuable information is collected by Bahl and Bhartia [16]. These authors are by no means exhaustive, but their work are particularly helpful in the prediction of the performance of specific microstrip circular disk antenna designs.

Several techniques have been developed for analysing microstrip antenna and the accuracy of each of them is based upon the factors it incorporates. Nevertheless, three commonly used techniques are the transmission line model, the modal-expansion cavity model, and the numerical method.

Derneryd [3,9,12] was the first to introduce the transmission line model for rectangular patches. The radiating element is considered as two slots perpendicular to the feed line separated by a transmission line of low characteristic impedance. The slots are characterized by their radiation pattern, directivity, and equivalent admittance. Recently, Bhattacharyya [19] devised a generalised transmission line model which is capable of solving all regular geometric patch shapes by means of a circuit model.

A mathematical analysis of a wide variety of microstrip patch shapes was published by Lo et al. [13,14] who used the modal-expansion cavity model to analyse rectangular, circu-

lar, semicircular, and triangular patch shapes. The field, confined within the hypothetical magnetic wall, between the patch and the ground plane is expanded in terms of a series of cavity resonant modes or eigenfunctions along with its eigenvalues or resonant frequencies associated with each mode.

For some irregular patch shapes where the appropriate orthogonal mode vectors are difficult to find, direct numerical analysis becomes more suitable than the modal-expansion technique. Agrawal and Bailey [6] developed a wire grid model to compute the grid segment currents. The finer the grid size, the better the approximation. However this numerical and empirical combined approach is cumbersome and excessively demanding of computer time. The method of moments, advanced by Newman and Tulyathan [18], is used to determine unknown surface currents flowing on the microstrip patch model and volume polarization currents for the dielectric slab. A system of N simultaneous linear equations is produced with coefficients given by an impedance matrix Z_{nm}. The technique successfully predicts the currents, impedance, and resonant frequency of the antenna provided the impedance matrix is precisely computed.

The more information on microstrip antennas is extracted, the better understanding on its applications is gained. Monolithic microstrip elements can be arranged in an array formation [1,2,3] for a fixed beam purpose, scanning effect,

wide angle coverage, and multiple frequency operations as long as low radiated power is not the restrictions. It is extremely preferable in airborne and satellite communications due to its lightweight and conformality. According to the array theory, it is necessary to have a very close element spacing in order to avoid grating lobes. However, the closer the element spacing, the more dominant is the coupling effect [21,22]. Besides, a minimum spacing required by the matching network and the feeding component always place a limit on how closely the element can be spaced. Disregarding the packaging problem, the mutual coupling effect plays a key role in the design of a microstrip array. The future of the microstrip antenna and array is so promising that it is jeopardizing the fate of its conventional counterparts.

1.3 OUTLINE OF THE THESIS

This thesis is divided into six chapters. Only the circular microstrip element is studied because of its simple geometry that makes the mathematics less complicated. Some basic concepts on microstrip antennas and their development are described in the introduction chapter. Chapter II relates the effective aperture voltage and the applied voltage in a matrix form. The input impedance and the array factor are also discussed. Mutual coupling calculation, based on the reaction concept, starts as the main topic in chapter

III. Both self and mutual admittance parameters are defined and formulated. Knowing the characteristics of the circular disc, the study is extended to the performance prediction of a microstrip array. An array of circular disc in a hexagonal shape is the prime objective of chapter IV. A set of pattern plots are produced, with the element spacing and dielectric constant as varying parameters, for comparison and design consideration. Before reaching the conclusion chapter, a multiple layer stack microstrip is also investigated in chapter V for the gain and the pattern improvement.

Chapter II

MICROSTRIP ANTENNA ARRAY THEORY

2.1 INTRODUCTION

An antenna array is employed and designed to satisfy all the required specifications of which a single radiator fails to produce such as gain, pattern, and peak angle. However, each antenna radiates differently from its isolated existence with the addition of some other antennas in its vicinity. As a matter of fact, coupling exists between neighboring radiating elements. It alters the active input impedance of each element, and therefore, changes the corresponding excitation voltage. Since the applied voltage is shared by the source internal impedance and the active input impedance of the antenna, the effective voltage at the antenna input, responsible for radiation, depends upon the active input impedance of the antenna. It is always important to know the properties of the excitation voltage and the active input impedance for each radiating element in an antenna array in order to predict its performance accurately. The formulation of the effective voltage and the active input impedance of each element of the array is presented in this chapter. The active input impedance is derived in terms of the mutual admittance and the applied voltages. The expression of the

array factor is also developed for a planar antenna array as a function of the orientations of the radiators and its associated effective voltages.

2.2 APPLIED VOLTAGE AND EFFECTIVE VOLTAGE

Consider a planar antenna array with n number of microstrip elements. Each open circuit element, according to Long [10], can be represented by a parallel RLC network in its input terminal. This lumped circuit is the input impedance of the element when viewed from the feeding terminal.

Let I_i and U_i be the current and the effective voltage at the input terminal, respectively, supplied by the source voltage V_i at the i-th radiating element as shown in Fig. 2. Assume that the coupling between elements does not affect

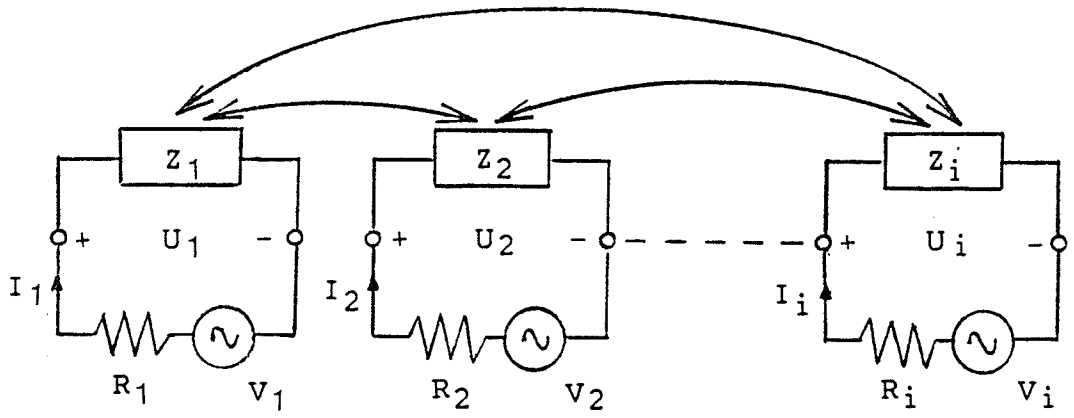

Figure 2: Equivalent circuit model of a microstrip array

any other modes except the operating mode. Thus, I_i and U_j can be related linearly[23] as follows:

$$I_i = Y_{i1}U_1 + Y_{i2}U_2 + Y_{i3}U_3 + \cdots\cdots + Y_{in}U_n \qquad (2.1)$$

where $i=1,2,3,\cdots\cdots,n$. Y_{ij}, in general, is the mutual admittance between the i-th and j-th elements, and is the self admittance of the i-th element if j=i. The derivation of Y_{ij} for circular elements will be discussed in the next chapter. In matrix notation, equation 2.1 becomes

$$[I_i] = [Y_{ij}]\ [U_j] \qquad (2.2)$$

where $[I_i]$ and $[U_j]$ are column vectors of order n and $[Y_{ij}]$ is an n*n square matrix.

In order to relate the applied voltage and the effective voltage at the input terminal of the element, I_i is expressed in terms of the applied voltage V_i and the internal resistance R_i of the i-th source as

$$I_i = \frac{V_i - U_i}{R_i} \qquad (2.3)$$

Substituting equation 2.3 to 2.2, an expression between V_i and U_i is obtained as

$$[V_i] = [Y_{ij}R_i + \delta_{ij}]\ [U_i] \qquad (2.4)$$

where δ_{ij} is a Kronecker delta and is defined as

$$\delta_{ij} = 1\ , \quad i = j$$
$$= 0\ , \quad i \neq j$$

With the knowledge of the source distribution the effective voltage can be found using equation 2.4. Alternatively, the source distribution required for a specific radiation pattern can always be determined from its aperture field distribution or effective voltage distribution. For impedance matching, a unit product of $Y_{ii}R_i$ in equation 2.4 is required in order to locate the position of the coaxial feed on the patch. The feed locations for some of the basic mode orders of a circular disc for materials of different dielectric constant are tabulated in Appendix A.

2.3 ACTIVE INPUT IMPEDANCE

The active input impedance Z_i of the i-th element when viewed from its feeding terminal among the existence of other elements is given by [23]

$$Z_i = \frac{U_i}{I_i} \tag{2.6}$$

where both U_i and I_i are defined as in the previous section. Express the effective voltage U_i in terms of the applied voltage V_i and the mutual admittance Y_{ij}, equation 2.4 becomes

$$[U_i] = [Y_{ij}R_i + \delta_{ij}]^{-1} [V_i] \tag{2.7}$$

Using equation 2.3 and 2.6, the active input impedance can be rewritten as

$$Z_i = \frac{R_i U_i}{V_i - U_i} \tag{2.8}$$

A general expression is derived by substituting equation 2.7 to 2.8 which gives

$$Z_i = \frac{R_i [Y_{ij} R_i + \delta_{ij}]^{-1} [V_i]}{[V_i] - [Y_{ij} R_i + \delta_{ij}]^{-1} [V_i]} \tag{2.9}$$

By further manipulation, the active input impedance is obtained and represented in terms of V_i as

$$Z_i = \frac{\sum_{j=1}^{n} R_i T_{ij} V_j}{\sum_{j=i}^{n} V_j (\delta_{ij} - T_{ij})} \tag{2.10}$$

where

$$[T_{ij}] = [Y_{ij} R_i + \delta_{ij}]^{-1}$$

For maximum power transmission, it is desirable to have the active input impedance matched to the characteristic impedance of the transmission line. Unfortunately, it is extremely difficult to match all the elements in the array perfectly due to the interactions of mutual coupling between them. Several numerical results on active input impedance of a microstrip array are collected in Appendix B as examples.

2.4 ARRAY FACTOR

For a two dimensional array of n elements, the array factor is given by Ma [20] as

$$F(\theta,\phi) = \sum_{i=1}^{n} U_i e^{jk_0(\bar{r}\cdot\bar{r}_i)+\alpha_i} \tag{2.11}$$

where U_i is the amplitude excitation of the i-th element, α_i is the associated phase excitation, k_0 is the free space wavenumber($=2\pi/\lambda$) and $\bar{r}$ is a unit vector in radial direction and is given by

$$\bar{r} = \bar{x}\ \sin\theta\cos\phi + \bar{y}\ \sin\theta\sin\phi + \bar{z}\ \cos\theta \tag{2.12}$$

where $\bar{x}$, $\bar{y}$, and $\bar{z}$ are unit vectors along x, y, and z direction, respectively. $\bar{r}_i$ is the position vector for the i-th element and is given by

$$\bar{r}_i = \bar{x}\ x_i + \bar{y}\ y_i \tag{2.13}$$

where x_i and y_i are the x and y coordinates of the i-th element, respectively. For the main beam to point at the position (θ_0,ϕ_0) and with the elements progressively phased, α_i is expressed as

$$\alpha_i = -jk_0\sin\theta_0[x_i\cos\phi_0 + y_i\sin\phi_0] \tag{2.14}$$

The main beam might not peak according to the excitation phase as specified because of the pattern cancellation due to the array geometry and the mutual coupling between the elements.

2.5 SUMMARY

On account of the coupling effect between microstrip array elements, the effective aperture voltage of each element is formulated in terms of the applied voltages of all the array patches and can be arranged in a matrix formation. Those effective aperture voltages are mainly responsible for the gain pattern calculation. It is possible to have the input impedance of a microstrip disc to match the source internal impedance by choosing the feed point appropriately. The active impedance of an array element is derived in terms of the applied voltages and mutual admittance of the array and the internal resistance of its source supply. A basic expression of an array factor with a scanning ability is developed and used for the microstrip array.

Chapter III

MUTUAL COUPLING BETWEEN MICROSTRIP ANTENNAS

3.1 INTRODUCTION

Mutual coupling is generated inevitably from any antenna array. The coupling effects may produce increased side lobe levels, main beam squint, filled or shifted nulls, grating lobes, and array blindness at some scan angles. However it is also possible for mutual coupling to produce an improvement in side lobe levels for those cases where the coupling causes a further tapering of the array distribution function. It would therefore be of substantial value to be able to predict coupling effects on microstrip array performance. Some measured data on mutual coupling between two disk elements were published by Parks et al. [21] and Jedlicka et al. [22]. In microstrip antenna, it is believed to be caused by the simultaneous effects of interactions through both free space radiation and surface waves. The principle of mutual coupling is established in the concept of reaction by Harrington [17]. For simplicity, the influence of surface waves is neglected in this literature. This limits the substrate of the antenna to be of small electrical thickness and low permittivity. From a practical point of view this limitation is not very restrictive. Indeed most microstrip

antennas satisfy these conditions with relative permittivities of the order of 2.5 and substrate thickness up to $0.015\lambda_0$. Based on a cavity model the mutual coupling is considered as the coupling between two current loops around the patch surface. It is basically a function of the geometric orientations of any two radiating patches. The reaction between two radiating apertures is formulated in an integral form [24]. The mutual admittance is obtained by using the concept of reaction. The expression of self admittance is also developed.

3.2 MUTUAL COUPLING BETWEEN TWO RADIATING APERTURES

Consider a circular element of arbitrary radius backed by the substrate and rested on a ground plane. It is believed that for the substrate thickness much less than half a wavelength ($h \ll \lambda/2$), only transverse magnetic fields exist under the patch metallization. With no z variation, the E_z component, expressed in modal-expansion, and the corresponding magnetic components are given by

$$E_z = \sum_{nm}\sum A_{nm} J_n(k_{nm}\rho)\cos n\phi \tag{3.1a}$$

$$H_\phi = \frac{1}{j\omega\mu} \sum_{nm}\sum A_{nm} k_{nm} J_n'(k_{nm}\rho)\cos n\phi \tag{3.1b}$$

$$H_\rho = \frac{1}{j\omega\mu\rho} \sum_{nm}\sum n A_{nm} J_n(k_{nm}\rho)\sin n\phi \tag{3.1c}$$

where $n=0,1,2,\cdots$ is the number of the periodicity in the ϕ direction, $m=1,2,3,\cdots$ is the number of zeros of the field in radial direction, A_{nm} is the mode coefficient and k_{nm} is the wave number, $\mu=\mu_0\mu_r$ and μ_r is the relative permeability of the substrate, $J_n'(k_{nm}\rho)$ is the first derivative of the Bessel function $J_n(k_{nm}\rho)$ of order n with respect to its argument.

In a cavity model, the metallic patch serves as an electric wall and does not radiate energy. Radiation is assumed to take place on the aperture, as shown in Fig. 3, due to the fringing field. The surface magnetic current distribution on the aperture surface can be found as

$$\begin{aligned}\bar{M} &= 2\bar{E}x\bar{n} \\ &= \bar{\phi}\ 2E_z \end{aligned} \qquad (3.2)$$

where $\bar{n}$ is the unit vector normal to the aperture. The factor 2 in equation 3.2 is due to the image effect of the ground plane.

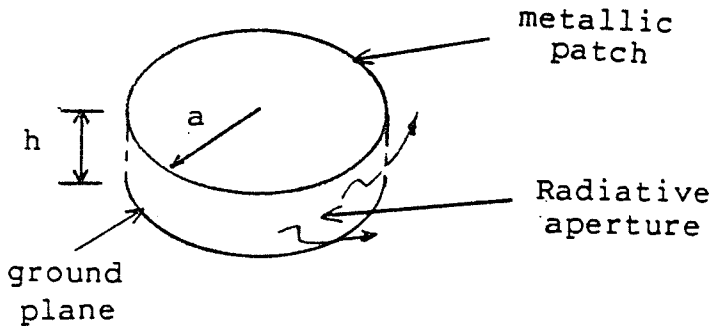

Figure 3: Radiative aperture of a microstrip patch

Since the substrate thickness is so thin that it is reasonable to assume the surface magnetic current distribution to be constant on the aperture of width h and the magnetic current is then given by

$$\bar{I}_m = h\bar{M}$$
$$= \bar{\phi}\ 2hE_z \tag{3.3a}$$

In cartesian coordinate, the magnetic current becomes

$$I_{mx} = -2hE_z\sin\phi \tag{3.3b}$$
$$I_{my} = 2hE_z\cos\phi \tag{3.3c}$$

Consider a magnetic current of radius ρ=a and centered at $(x_i, y_i, 0)$ as shown in Fig. 4, the electric vector potential, generated by the magnetic current, observed from an arbitrary observation point P(x',y',z'), is given by

$$\bar{F}(r) = \frac{\epsilon_0}{4\pi r} e^{-jk_0 r} \int_v \bar{J}_m(r') e^{jk_0 \bar{r}\cdot\bar{r}'} dr'$$

$$dF_{x'} = \frac{\epsilon_0}{4\pi r_1} e^{-jk_0 r_1} I_{mx} a d\phi \tag{3.4a}$$

$$dF_{y'} = \frac{\epsilon_0}{4\pi r_1} e^{-jk_0 r_1} I_{my} a d\phi \tag{3.4b}$$

$$dF_{z'} = 0 \tag{3.4c}$$

where $r_1^2 = [(x'-a\cos\phi-x_i)^2+(y'-a\sin\phi-y_i)^2+z'^2]$ is the distance from the current source to the observation point and $\bar{J}_m(r')$ is the magnetic current distribution. The electric field $d\bar{E}$ experienced at the observation point can readily be

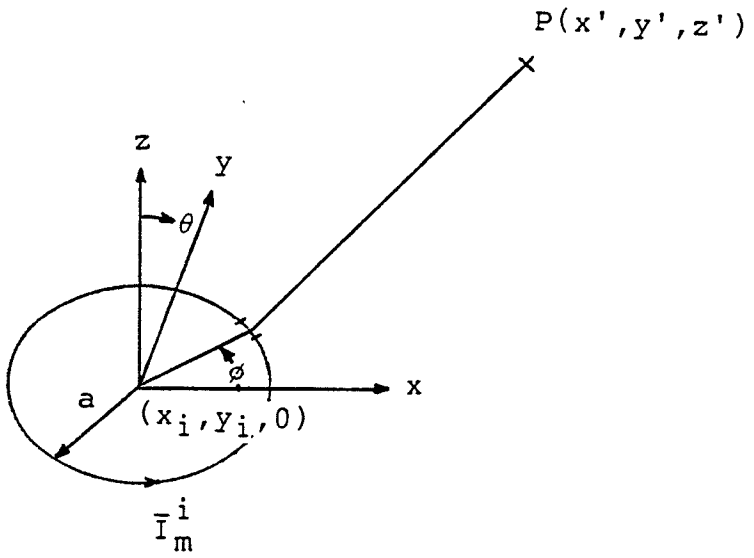

Figure 4: A magnetic ring current modelling of a microstrip circular disc

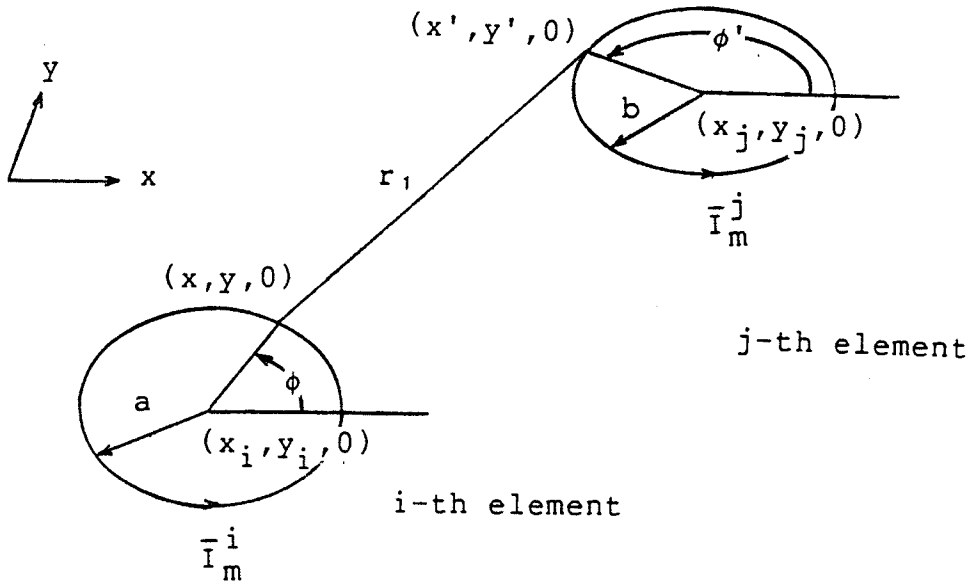

Figure 5: A schematic diagram of two co-planar magnetic current ring

obtained from

$$\bar{dE} = -\frac{1}{\epsilon_0}\bar{\nabla}\times\bar{dF}$$

which gives

$$dE_{x'} = -\frac{I_{my}ad\phi}{4\pi r_1^3}e^{-jk_0r_1}(1+jk_0r_1)z' \tag{3.5a}$$

$$dE_{y'} = \frac{I_{mx}ad\phi}{4\pi r_1^3}e^{-jk_0r_1}(1+jk_0r_1)z' \tag{3.5b}$$

$$dE_{z'} = \frac{I_{m}ad\phi}{4\pi r_1^3}e^{-jk_0r_1}(1+jk_0r_1)(x'\cos\phi+y'\sin\phi-a) \tag{3.5c}$$

If the observation point P lies along another magnetic current source located at $(x_j,y_j,0)$ with radius b illustrated as in Fig. 5, the azimuthal component of the magnetic field at any point along the j-th element aperture can be evaluated at z'=0 from the Maxwell's equation as follows:

$$dH_{x'}\Big|_{z'=0} = -\frac{1}{j\omega\mu}\frac{I_{m}ad\phi}{4\pi r_1^3}e^{-jk_0r_1}\left[2\sin\phi(1+jk_0r_1) + \frac{(x'\cos\phi+y'\sin\phi-a)(y'-a\cos\phi)}{r_1^2}(\{k_0r_1\}^2-j3k_0r_1-3)\right] \tag{3.6a}$$

$$dH_{y'}\Big|_{z'=0} = -\frac{1}{j\omega\mu}\frac{I_{m}ad\phi}{4\pi r_1^3}e^{-jk_0r_1}\left[2\cos\phi(1+jk_0r_1) + \frac{(x'\cos\phi+y'\sin\phi-a)(x'-a\cos\phi)}{r_1^2}(\{k_0r_1\}^2-j3k_0r_1-3)\right] \tag{3.6b}$$

where $x'=b\cos\phi'+x_j$, $y'=b\sin\phi'+y_j$. In cylindrical coordinate, the magnetic field component is expressed as

$$dH_{\phi'} = -dH_{x'}\sin\phi' + dH_{y'}\cos\phi' \tag{3.7}$$

The total magnetic field experienced by the j-th element and induced by the i-th element is

$$H^t_{\phi'} = \int_{\phi=0}^{2\pi} dH_{\phi'} \tag{3.8}$$

Appling the concept of reaction [17], the reaction on the edge of the j-th current source due to the i-th one is defined by

$$\frac{1}{2}\langle i,j\rangle = -\iint_S \bar{H}_{ij}\cdot\bar{M}_j\, ds \tag{3.9}$$

The integration is taken over S , the aperture area of the j-th element with the assumption that $H^t_{\phi'}$ is constant on the aperture surface, and $ds=hbd\phi'$. Hence

$$\langle i,j\rangle = -2hb\int_0^{2\pi} H^t_{\phi'}E^j_z\, d\phi' \tag{3.10}$$

where E^j_z is the E_z component under the patch region of the j-th element of radius b. Further manipulation gives

$$\langle i,j\rangle = \frac{jabh^2E_aE_b}{2\pi k_0\eta_0}\int_0^{2\pi}\int_0^{2\pi}\cos n\phi\cos n\phi' F(r_1,\phi,\phi')d\phi d\phi' \tag{3.11}$$

where

$$F(r_1,\phi,\phi') = \frac{1}{r_1^3} e^{-jk_0 r_1} \Big[2(1+jk_0 r_1)\cos(\phi-\phi') + \frac{(x'\cos\phi+y'\sin\phi-a)[y'\sin\phi'+x'\cos\phi'-a\cos(\phi'-\phi)]}{r_1^2} \cdot\{(k_0 r_1)^2-j3k_0 r_1-3\} \Big] \quad (3.12a)$$

$$E_a = A_{nm}J_n(k_{nm}a) \quad (3.12b)$$

$$E_b = A_{nm}J_n(k_{nm}b) \quad (3.12c)$$

The expression <i,j> gives the reaction of the i-th element on the j-th element of arbitrary radii under any operating mode of interest. For two identical circular patches with radius a, equation 3.11 becomes

$$\langle i,j\rangle = \frac{ja^2h^2E_a^2}{2\pi k_0\eta_0} \int_0^{2\pi}\int \cos n\phi \cos n\phi' F(r_1,\phi,\phi')\,d\phi\,d\phi' \quad (3.13)$$

where r_1 becomes

$$r_1^2 = (x'-x)^2+(y'-y)^2$$
$$= (a\cos\phi'+x_j-a\cos\phi-x_i)^2+(a\sin\phi'+y_j-a\sin\phi-y_i)^2 \quad (3.14)$$

3.3 MUTUAL ADMITTANCE

The coupling between two patches is represented as mutual admittance in this section. The reaction of patch a on b with constant electric and magnetic component on the aperture can be expressed as

$$\begin{aligned} <i,j> &= 2\int E_z^i H_\phi^{ij} ds \\ &= 2\pi a h E_a H_{ab} \\ &= 2\pi a h E_a E_b Y_{ij} \end{aligned} \tag{3.15}$$

where Y_{ij} is the mutual admittance of patch i on j. E_a and E_b are the amplitude of the aperture electric fields of the i-th and j-th patches, respectively, which were defined in equation 3.12. The stationary expression for the mutual wall admittance can be defined as[23]

$$Y_{ij}^W = \frac{<i,j>}{2\pi a h E_a E_b} \tag{3.16}$$

The stationary expression for the mutual admittance takes the form

$$Y_{ij} = \frac{<i,j>}{2U_c^i U_d^j} \tag{3.17}$$

which U_c^i and U_d^j are the effective voltages at the input terminal of patch i and j, respectively.

$$U_c^i = -hE_c^i \tag{3.18a}$$

$$U_d^j = -hE_d^j \tag{3.18b}$$

where $E_c^i = A_{nm} J_n(k_{nm} c)$ and $E_d^j = A_{nm} J_n(k_{nm} d)$ with c and d the feed positions of the i-th and j-th patches, respectively. Hence, the relation between the mutual wall admittance and the mutual admittance is

$$Y_{ij} = \frac{\pi a}{h} \frac{J_n^2(k_{nm} a)}{J_n^2(k_{nm} c)} Y_{ij}^w \tag{3.19}$$

It can be shown that the reaction of i on j is the same as that of j on i as the reciprocity holds. That implies

$$Y_{ij} = Y_{ji} \tag{3.20}$$

Fig. 6 illustrates the variation of the mutual admittance between two identical circular disc, arranged in different orientations, as their separation is varied. The characteristics of the mutual admittance, normalized to the self wall conductance of the patch at resonance, exhibit good agreement with Bhattacharyya [24]. They are similar to the characteristics of a damped oscillation. The closer the patches, the greater their mutual coupling. It decays as the separation between the patches increases. It is apparent that coupling effect is contributed largely by the E-plane arrangement (Fig. 6a) rather than the H-plane configuration (Fig. 6b). Unfortunately, a minimum mutual conductance value correlates to a slightly off value of maximum mutual susceptance and vice versa, it is unlikely to resolve an optimized position where mutual coupling is ineffective.

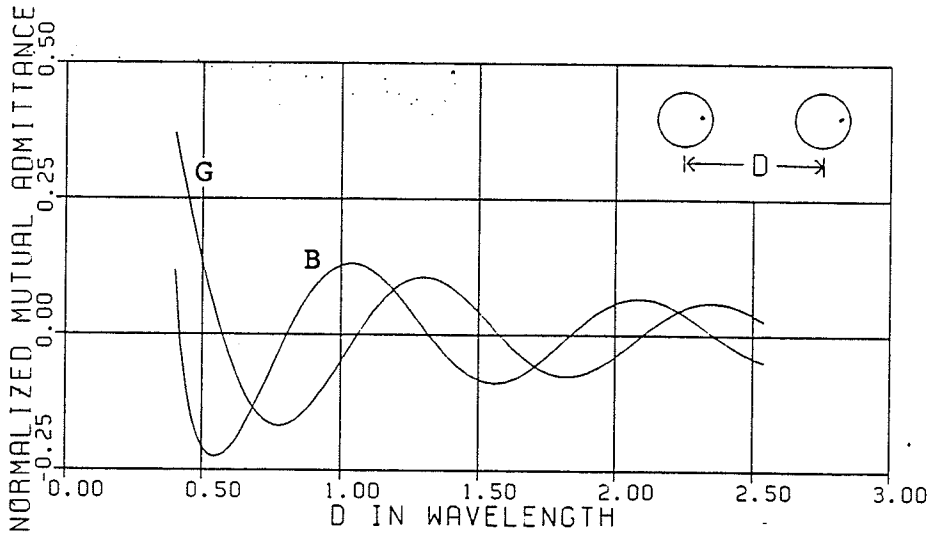

(a) E-plane coupling

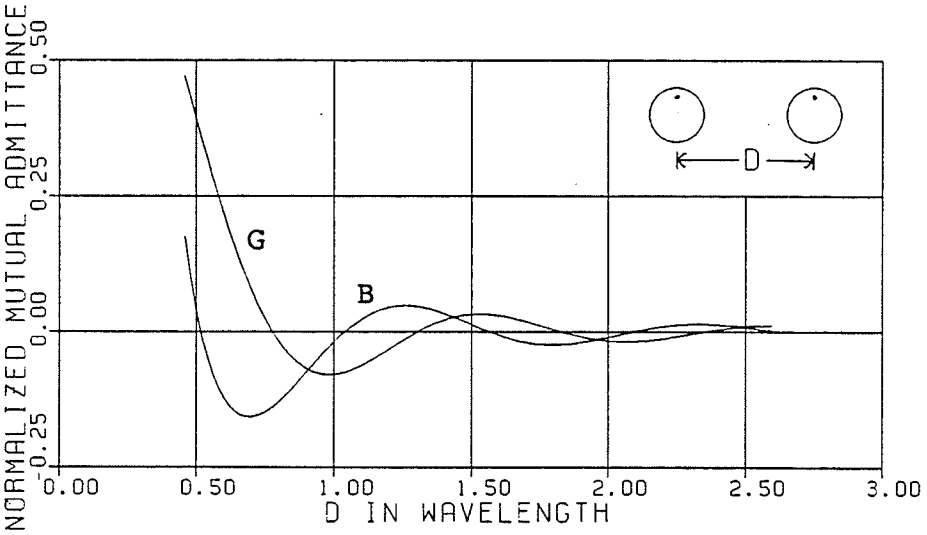

(b) H-plane coupling

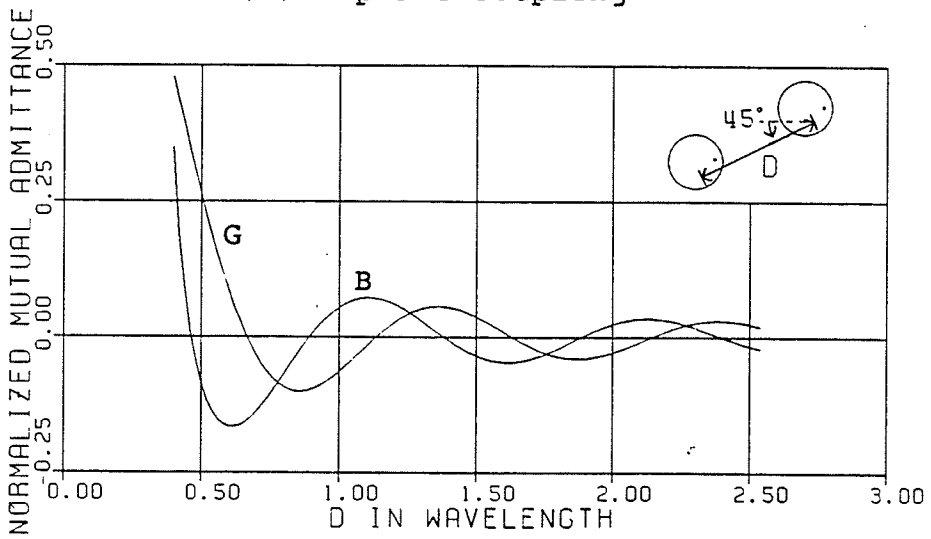

(c) Mutual coupling at intercordinal plane, ϕ=45°

Figure 6: Mutual admittance (normalized to the self wall conductance) for various separation orientations

3.4 SELF ADMITTANCE

The self admittance Y_{ii} of a microstrip disc can be determined from the mutual admittance expression in equation 3.15 by writing j=i with $x_i=y_i=0$. However the evaluation of the integral results with a singularity whenever $\phi=\phi'$. This is due to the assumption of the infinitely thin line current source where, in reality, it should be a surface current source with width h. The self wall conductance is obtained after removing the singularity by finding the limit at ϕ' using the L'Hospital's rule. It is given by equation 3.21 and its characteristic, normalized to the product of the patch radius and the thickness of the substrate, is plotted against the operating frequency as shown in Fig. 7.

$$G_a = \frac{ah}{2\pi^2 k_0 \eta_0} \int_0^{2\pi} \cos n\phi \cos n\phi' G(r_1,\phi,\phi') d\phi d\phi' \qquad (3.21)$$

where

$$G(r_1,\phi,\phi') = \frac{1}{r_1^3}\left[\{1+\cos^2(\frac{\phi-\phi'}{2})\}\{\sin(k_0 r_1)-k_0 r_1 \cos(k_0 r_1)\} - k_0^2 r_1^2 \sin^2(\frac{\phi-\phi'}{2})\sin(k_0 r_1)\right] \qquad (3.22a)$$

$$r_1 = \left|2a\sin(\frac{\phi-\phi'}{2})\right| \qquad (3.22b)$$

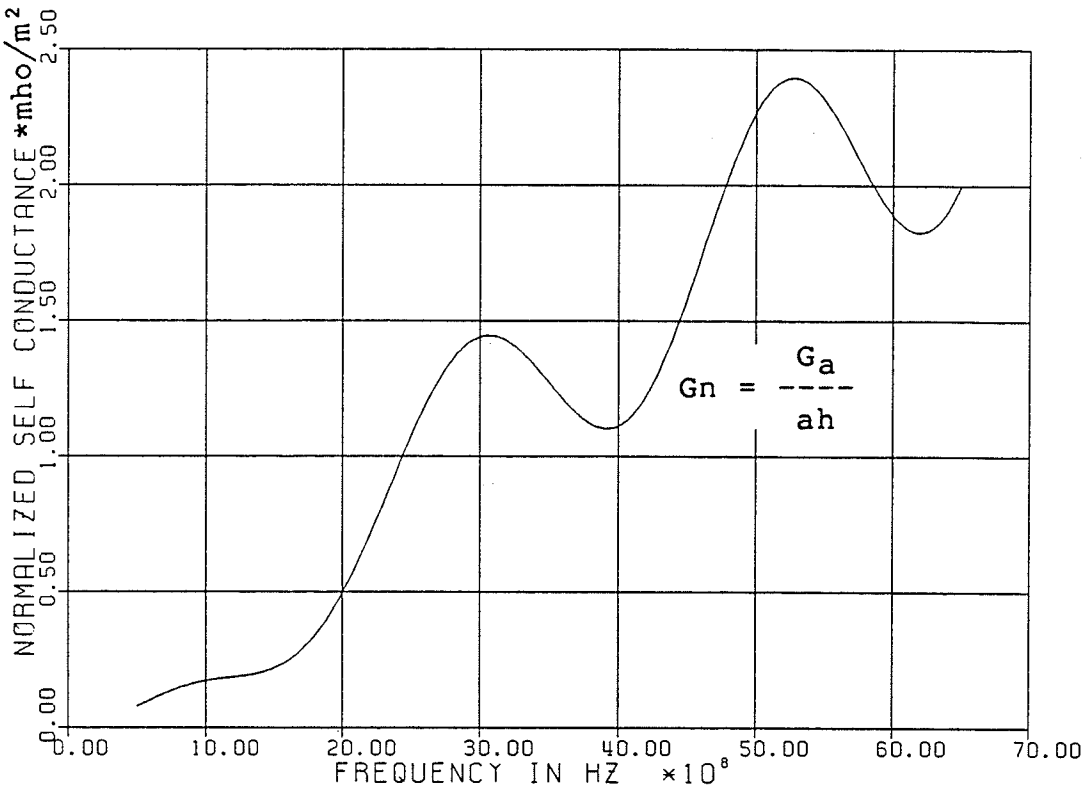

Figure 7: Normalized self wall conductance of a microstrip disc versus its operating frequency

Since the singularity of the self susceptance is irremovable, it has to be calculated separately. For simplicity, it is assumed that the total energy stored between the disc and the ground plane is a combination of the energy under the patch metallization ($\rho \leq a$) and the energy stored in the fringing fields ($a_e \leq \rho < a$). The effective radius a_e of a circular disc is given by Chew and Kong [15] as

$$a_e^2 = a^2(1+\Delta) \tag{3.23}$$

where

$$\Delta = \frac{2h}{\pi \epsilon_r a}\left[\ln\left(\frac{a}{2h}\right)+1.41\epsilon_r+1.77+\frac{h}{a}(0.268\epsilon_r+1.65)\right] \tag{3.24}$$

The total stored energy can be estimated using the cavity model theory. The wave equation in z direction under the metallization takes on the form

$$\nabla^2 E_z + k_1^2 E_z = j\omega\mu J_z \tag{3.25}$$

where k_1 is the wavenumber in the dielectric substrate and ϵ_r is the relative permittivity of the dielectric material. J_z is the z-directed electric current density and for a probe fed antenna, it is given by

$$J_z = I_0 \frac{\delta(\rho-c)}{c} \delta(\phi-\phi_0) \tag{3.26}$$

where I_0 is the total current supplied by the feed probe located at $\rho=c$ and $\phi=\phi_0$. The electric component E_z is expanded as a summation of orthogonal eigenfunctions as in equation 3.1a. Thus

$$E_z = \sum_{nm}\sum A_{nm} J_n(k_{nm}\rho)\cos n\phi \tag{3.27}$$

with the boundary condition $J_n'(k_{nm}a_e)=0$. The notations in equation 3.27 are the same as those in section 3.2. Substitute equation 3.27 into 3.25 and solve the expression in cylindrical coordinate by using the properties of the Fourier Bessel differential equation, equation 3.25 can be written as

$$\sum_{nm}\sum A_{nm}(k_1^2-k_{nm}^2) J_n(k_{nm}\rho)\cos n\phi = j\omega\mu J_z \tag{3.28}$$

The mode coefficient A_{nm} can be extracted by taking a Fourier-Bessel integration on the patch surface on both sides of equation 3.28. Thus

$$A_{nm} = \frac{j\omega\mu \int_0^{2\pi} \int_0^{a_e} J_z J_n(k_{nm}\rho)\cos n\phi\,\rho\,d\rho\,d\phi}{\sigma_n(k_1^2 - k_{nm}^2) \int_0^{a_e} J_n(k_{nm}\rho)\rho\,d\rho} \tag{3.29}$$

where $\sigma_n=1$ for $n\neq 0$ and $\sigma_0=2$. Subject to the boundary condition, the analytical solution for equation 3.29 becomes

$$A_{nm} = \frac{j2k_0\eta_0 I_0 J_n(k_{nm}c)\cos n\phi_0}{\sigma_n\pi(k_0^2 - k_{nm}^2)\left[1 - \frac{n^2}{(k_{nm}a_e)^2}\right]\left[a_e J_n(k_{nm}a_e)\right]^2} \tag{3.30}$$

A general expression of the mode coefficient is thus established for different operating mode. It is understood that when the operating frequency is close to any resonant mode, $k_1^2 - k_{nm}^2 = 0$. The term containing A_{nm} corresponds to that resonant mode will be dominant and other terms will be negligibly small. E_z can thus be approximated as

$$E_z(\theta,\phi) = A_{nm} J_n(k_{nm}\rho)\cos n\phi \tag{3.31}$$

The cavity is no longer a radiator, but a resonator. The input impedance seen by the feed can be represented by

$$jB = \frac{I_0}{-hE_z(c,0)} \tag{3.32}$$

Use the result in equation 3.30 and have it substituted into equation 3.31 and then 3.32, the self susceptance is obtained to be

$$B = \frac{\pi\sigma_n(k_1^2-k_{nm}^2)a_e^2}{2\omega\mu h}\left[1 - \frac{n^2}{(k_{nm}a_e)^2}\right]\left[\frac{J_n(k_{nm}a_e)}{J_n(k_{nm}c)}\right]^2 \qquad (3.33)$$

Since the cavity is assumed to be an ideal resonator, no energy is dissipated and, therefore, the input impedance is purely imaginary. The resonant frequency of the resonator is given by

$$f_0 = \frac{cX_{nm}}{2\pi a_e\sqrt{\epsilon_r}} \qquad (3.34)$$

where X_{nm} is the m-th zero of the derivative of the Bessel function of order n and c is the velocity of light in free space.

The self wall susceptance for each mode can be evaluated from the electric (W_e^{nm}) and magnetic (W_h^{nm}) stored energy in the fringe of the disk [25] and is given by

$$B_a = \frac{2\omega(W_e^{nm} - W_h^{nm})}{\frac{1}{2}\int_s |E_z^{nm}|^2\, ds} \qquad (3.35)$$

where

$$W_e^{nm} = \int_{\Delta v} \frac{\epsilon}{4} |E_z^{nm}|^2\, dv \qquad (3.36a)$$

$$W_h^{nm} = \int_{\Delta v} \frac{\mu}{4} \left(|H_\rho^{nm}|^2 + |H_\phi^{nm}|^2 \right) dv \qquad (3.36b)$$

with E_z^{nm}, H_ρ^{nm}, and H_ϕ^{nm} are given by equation 3.1. The term $dv=\rho d\rho d\phi dz$ covers the entire fringing volume and $ds=\rho d\phi dz$ includes the whole aperture surface. Since the radius extension due to the fringing field is so small that it is reasonable to assume the tangential electric and magnetic fields to be constant at the region $a \le \rho \le a_e$. Substituting equation 3.36 to 3.35, the self wall susceptance becomes

$$B_a = \frac{\omega \pi h [\epsilon |E_{za}|^2 - \mu \{ |H_{\rho a}|^2 + |H_{\phi a}|^2 \} \int_a^{a_e} \rho d\rho]}{\pi a h |E_{za}|^2} \qquad (3.37)$$

where

$$E_{za} = A_{nm} J_n(k_{nm} a) \qquad (3.38a)$$

$$H_{\phi a} = \frac{A_{nm} k_{nm}}{j\omega\mu} J_n'(k_{nm} a) \qquad (3.38b)$$

$$H_{\rho a} = \frac{A_{nm} n}{j\omega\mu a} J_n(k_{nm} a) \qquad (3.38c)$$

Further simplification gives

$$B_a = \left[k_1^2 - \frac{n^2}{a^2} - \frac{k_{nm}^2 J_n'^2(k_{nm} a)}{J_n^2(k_{nm} a)} \right] \frac{(a_e^2 - a^2)}{2 k_o \eta_o a} \qquad (3.39)$$

Hence, the self wall (boundary) admittance is

$$Y_a = G_a + jB_a \qquad (3.40)$$

where G_a was defined as in equation 3.21.

3.5 SUMMARY

A microstrip radiating aperture is modelled by a magnetic current ring with its current induced by a longitudinal electric field inside the microstrip substrate. The electric field E_z, expanded in modal-expansion, is assumed to be the sole electric component under the patch. Reaction between any two magnetic current rings of arbitrary dimensions is deduced and their mutual admittance can be evaluated by applying the reaction concept. It has been shown that E-plane coupling produces a greater influence on the microstrip array than the H-plane coupling. The self admittance, bears a movable singularity, can also be obtained from the reaction expression. The self susceptance can be found by treating the microstrip disc as an ideal resonator with an extended radius to incorporate the fringing field.

Chapter IV

RADIATION PATTERN OF MICROSTRIP ARRAY

4.1 INTRODUCTION

Mutual coupling between radiating elements in microstrip arrays results in both distortion of the element radiation and errors in the element feeding voltages. In scanned arrays, these effects are scan angle sensitive. The significance of the influence depends on the array geometry and its application. Nevertheless, the radiation pattern of a microstrip array accounts on the radiating apertures of each element. It may be obtained from various assumed current conditions and distributions along the antenna structure [16]. Due to the finite width of the radiating aperture, both electric and magnetic currents are assumed on the aperture. The aperture extends from the top patch to the bottom ground plane and encircles the patch around the circumference with a width h which is the depth of the substrate. With the existence of both types of sources the resultant field is a superposition of that produced by the electric source and magnetic source separately. When the knowledge of the electric and magnetic currents is known, the magnetic and electric vector potentials can be derived [16,17]. The electric far field can be written in terms of the electric

and magnetic vector potentials. Once the field radiation is clear, all other antenna parameters may be readily obtained.

4.2 RADIATION PATTERN OF A SINGLE CIRCULAR PATCH

The total array pattern is the product of the element pattern and the array factor. The expression of the array factor was derived in section 2.4. The element pattern will be formulated in this section.

It is understood that radiation of a microstrip antenna is primarily due to the effect of fringing fields. These fringing fields induce both the magnetic and electric currents on the aperture at ρ=a. The far field radiation can be determined subject to the knowledge of those induced currents. Assume that only the TM_{nm} mode can be hold inside the microstrip cavity, the electric field on the aperture surface is given by [23]

$$E_z = E_a \cos n\phi \tag{4.1}$$

where $E_a = A_{nm} J_n(k_{nm}\rho)$. The tangential magnetic field on the aperture will thus be

$$H_\phi = -Y_a E_a \cos n\phi \tag{4.2}$$

where Y_a is the self wall admittance of the radiating aperture and has derived earlier in equation 3.40.

If the dielectric material is assumed to be isotropic, homogeneous, and lossless, and the conductivities of the microstrip conductor and ground plane are infinite, the surface currents can be written in terms of tangential electric and magnetic fields as

$$\bar{K} = 2\bar{n}x\bar{H} = 2\ \bar{\rho}x\bar{\phi}\ H_{\phi}$$
$$= \bar{z}\ 2H_{\phi} \tag{4.3a}$$
$$\bar{M} = 2\bar{E}x\bar{n} = 2\ \bar{z}x\bar{\rho}\ E_{z}$$
$$= \bar{\phi}\ 2E_{z} \tag{4.3b}$$

where $\bar{\rho}$, $\bar{\phi}$, and $\bar{z}$ are the unit vectors along the ρ, ϕ, and z directions, respectively. $\bar{n}$ is the unit normal to the aperture surface. The factor 2 accounts for the image with respect to the ground plane. Practical ground planes are usually several wavelengths in dimension so that the assumption of an infinite ground plane is justified for calculating the far field patterns. However for angles near the ground plane, edge diffraction effects should be considered.

The derivations of the magnetic and electric vector potentials are presented in Appendix C and they are, respectively, given by

$$\bar{A} = \frac{\mu}{4\pi r} e^{-jk_0 r} \int_0^h \int_0^{2\pi} \bar{K}(\phi') e^{jk_0 a\sin\theta\cos(\phi'-\phi)}\, a\,d\phi\,dz \tag{4.4a}$$

$$\bar{F} = \frac{\epsilon}{4\pi r} e^{-jk_0 r} \int_0^h \int_0^{2\pi} \bar{M}(\phi') e^{jk_0 a\sin\theta\cos(\phi'-\phi)}\, a\,d\phi\,dz \tag{4.4b}$$

For convenience in far field calculation, equation 4.4 is transformed from cylindrical to spherical coordinates with the help of the following transformation relation.

$$\begin{bmatrix} T_r \\ T_\theta \\ T_\phi \end{bmatrix} = \begin{bmatrix} \sin\theta\cos(\phi'-\phi) & -\sin\theta\sin(\phi'-\phi) & \cos\theta \\ \cos\theta\cos(\phi'-\phi) & -\cos\theta\sin(\phi'-\phi) & -\sin\theta \\ \sin(\phi'-\phi) & \cos(\phi'-\phi) & 0 \end{bmatrix} \begin{bmatrix} T_{\rho'} \\ T_{\phi'} \\ T_{z'} \end{bmatrix} \tag{4.5}$$

The transverse components of the vector potential are then determined as

$$A_\theta = \frac{\mu a h Y_a E_a}{2\pi r} e^{-jk_0 r} \sin\theta \int_0^{2\pi} G(\theta,\phi,\phi')\, d\phi' \tag{4.6a}$$

$$A_\phi = 0 \tag{4.6b}$$

$$F_\theta = -\frac{a h \epsilon_0 E_a}{2\pi r} e^{-jk_0 r} \cos\theta \int_0^{2\pi} \sin(\phi'-\phi) G(\theta,\phi,\phi')\, d\phi' \tag{4.6c}$$

$$F_\phi = \frac{a h \epsilon_0 E_a}{2\pi r} e^{-jk_0 r} \int_0^{2\pi} \cos(\phi'-\phi) G(\theta,\phi,\phi')\, d\phi' \tag{4.6d}$$

where

$$G(\theta,\phi,\phi') = \cos n\phi' e^{jk_0 a \sin\theta \cos(\phi'-\phi)}$$

By means of superposition, the total radiated electric far field or the element pattern can be deduced as

$$E_\theta = E_\theta^e + E_\theta^m = -j\omega A_\theta - j\omega\eta_0 F_\phi \tag{4.7a}$$

$$E_\phi = E_\phi^e + E_\phi^m = -j\omega A_\phi - j\omega\eta_0 F_\theta \tag{4.7b}$$

After performing the mathematics involved in the above equations, the analytical solution of the element pattern is obtained as follows:

$$E_\theta^e = \gamma[-j2\eta_0 Y_a J_n(X)\sin\theta]\cos n\phi \quad (4.8a)$$

$$E_\theta^m = \gamma[J_{n+1}(X)-J_{n-1}(X)]\cos n\phi \quad (4.8b)$$

$$E_\phi^e = 0 \quad (4.8c)$$

$$E_\phi^m = \gamma[J_{n+1}(X)+J_{n-1}(X)]\cos\theta\sin n\phi \quad (4.8d)$$

where

$$\gamma = \left(\frac{k_0 ah}{2r}\right)e^{-jk_0 r}\, j^n E_a$$

$$X = k_0 a\sin\theta$$

and $E_a = 1$ as the excitation coefficients have already been incorporated in the array factor.

4.3 RADIATION PATTERN OF A MICROSTRIP ANTENNA ARRAY

Microstrip arrays are ideally suited to many applications requiring narrow bandwidth (a few percent at the most), low power,and extreme lightweight or conformality. A linear array can be constructed easily for various applications and as well as a two dimensional array if sufficient area is available. A hexagonal array consists of seven circular microstrips is studied in this section. Both linear and circular polarizations will be discussed in terms of the directive gain of the array.

4.3.1 Power gain calculation

In order to determine the gain, the total radiated power of the array must be computed in advance. Power radiates through the aperture surface according to its own generated currents and also through its interactions with other antennas due to mutual coupling. The average power radiated by an antenna is given by

$$P_{av} = \frac{1}{2} \oint_s \text{Real}(\bar{E} \times \bar{H}^*) \cdot \bar{ds} \tag{4.9}$$

where the integration is over the radiating surface. The notation * represents the conjugate value of the component. If E_z^i is the aperture electric field for the i-th element, the average power radiated by the patch will be [23]

$$P_i = \frac{1}{2} \int_0^h \int_0^{2\pi} \text{Real}[E_z^i \times (H_\phi^i + \sum_{j \neq i}^{n} H_\phi^{ij})^*] \cdot ds \tag{4.10}$$

where H_ϕ^i is the self magnetic field and H_ϕ^{ij} is the magnetic field produced by the j-th source experienced by the i-th aperture. These magnetic and electric fields are related by means of their mutual reaction, a previously derived circuital parameter, and can be written as

$$H_\phi^{ij} = Y_{ij}^w E_z^j \tag{4.11}$$

where

$$Y_{ij}^w = -\frac{H_\phi^{ij}}{E_z^j} = \frac{<i,j>}{2\pi a h E_z^i E_z^j} \tag{4.12}$$

as given by equation 3.16. The power radiated by the i-th element can thus be expressed in terms of the circuit parameters subject to the circuit model in Chapter III. By writing equation 4.10 in terms of equation 4.11 and 4.12, and performing the integration over the aperture surface ds=adϕdz, it can be found that

$$P_i = \pi ah \; \text{Real}[E_z^i(\sum_{j=1}^{n} E_z^j Y_{ij})^*] \tag{4.13}$$

where $E_z^i=E_a^i$. Under an impedance matched case with no reflection, $Y_{ii}=G_{ii}$ and is real. Equation 4.13 becomes

$$P_i = \pi ah \; \text{Real}[E_z^i(E_z^j G_{ii}+\sum_{j\neq i}^{n} E_z^j Y_{ij})^*] \tag{4.14}$$

The total power radiated by the array will be

$$P_t = \sum_{i=1}^{n} P_i \tag{4.15}$$

The average power radiated per unit area is

$$P_r = \frac{P_t}{4\pi r^2} \tag{4.16}$$

where r is the distance from the reference origin to the observation point. The far field radiating power per unit area by the array can also be expressed as

$$P_{array} = \frac{|E_\theta|^2+|E_\phi|^2}{120\pi} \tag{4.17}$$

Hence the gain of the array with respect to an isotropic radiator becomes

$$G(\theta,\phi) = \frac{P_{array}}{P_r} \tag{4.18}$$

Alternatively, the total array power can also be calculated by integrating the field pattern over the upper hemispheric surface which is

$$P_t = \frac{1}{\eta} \int_s (|E_\theta|^2+|E_\phi|^2) r^2 \sin\theta d\theta d\phi \tag{4.19}$$

A comparison of the total radiated power (in watt) between the two methods is tabulated in Table 1 for a seven element array (page 49, ϵ_r=2.32, h=1.59mm, TM_{11}) in circular polarization with mutual coupling included.

Element spacing (λ)	Phase excitation θ_0	Phase excitation ϕ_0	Circuital parameter technique	Field pattern method	Difference percentage (%)
0.65	0^0	0^0	0.08104	0.08255	1.83
0.65	45^0	270^0	0.13080	0.16470	20.58
0.65	70^0	270^0	0.13270	0.11550	-14.89
0.70	0^0	0^0	0.09000	0.09370	3.95
0.70	45^0	270^0	0.13660	0.15460	11.64
0.70	70^0	270^0	0.13660	0.11058	-23.53

TABLE 1

A comparison of power P_t from two different methods

The percentage difference between the two methods is obtained with respect to the field pattern integration. In general, the field pattern integration is considered to be most involved in calculating the radiated power. Both methods agree with each other closely in the case of no scanning. The difference between them might due to the excitation of higher order modes and the circuit mismatch caused by the mutual coupling through scanning.

4.3.2 Gain in circular polarization

In transmission between mobile antennas such as those of missiles or satellites, the orientation cannot be controlled in some cases and the maximum polarization loss must be used in the link analysis. In order to avoid the loss due to polarization mismatch, circular polarized antennas are used in these cases. Circular polarization can be obtained by two orthogonal excitations in phase quadrature.

Two feeds are now considered to be located at $\phi=0°$ and $\phi=90°$ with a phase difference of 90° and their associated field components are E_θ^1, E_ϕ^1, and E_θ^2, E_ϕ^2, respectively. These field pattern are found to be

$$E_\theta^1 = f(\theta)\cos n\phi \qquad (4.20a)$$

$$E_\phi^1 = g(\theta)\sin n\phi \qquad (4.20b)$$

$$E_\theta^2 = jf(\theta)\sin n\phi \qquad (4.20c)$$

$$E_\phi^2 = -jg(\theta)\cos n\phi \qquad (4.20d)$$

where

$$f(\theta) = E_\theta$$

$$g(\theta) = E_\phi$$

and both E_θ and E_ϕ are described in equation 4.7. The total pattern is the summation of the field patterns due to both feeds. They are given by

$$E_\theta = E_\theta^1 + E_\theta^2 = f(\theta)e^{j\phi} \tag{4.21a}$$

$$E_\phi = E_\phi^1 + E_\phi^2 = -jg(\theta)e^{j\phi} \tag{4.21b}$$

Taking the right-hand and left-hand polarizations as the co-polar and cross-polar components, respectively, and hence

$$\bar{E}_{co} = A(\theta,\phi)\left[\frac{\bar{\theta}+j\bar{\phi}}{2}\right] \tag{4.22a}$$

$$\bar{E}_x = B(\theta,\phi)\left[\frac{\bar{\theta}-j\bar{\phi}}{2}\right] \tag{4.22b}$$

where the amplitude of $A(\theta,\phi)$ and $B(\theta,\phi)$ are given by the following equations [23]:

$$2|A(\theta,\phi)|^2 = \{|f(\theta)|^2+|g(\theta)|^2+2|f(\theta)||g(\theta)||\sin(\theta_f-\theta_g)|\} \tag{4.23a}$$

$$2|B(\theta,\phi)|^2 = \{|f(\theta)|^2+|g(\theta)|^2-2|f(\theta)||g(\theta)||\sin(\theta_f-\theta_g)|\} \tag{4.23b}$$

With both θ_f and θ_g being the phase angles of $f(\theta)$ and $g(\theta)$, respectively. The gain pattern for co-polar and cross-polar components with respect to isotropic radiation are

$$G_{co}(\theta,\phi) = \frac{4\pi r^2 |A(\theta,\phi)|^2}{120\pi \cdot 2P_t} \qquad (4.24a)$$

$$G_x(\theta,\phi) = \frac{4\pi r^2 |B(\theta,\phi)|^2}{120\pi \cdot 2P_t} \qquad (4.24b)$$

$2P_t$ is used in equation 4.24 accounts for the two feed voltages, each of which radiates P_t amount of power.

4.4 NUMERICAL RESULTS AND DISCUSSIONS

4.4.1 Radiation pattern of a seven element array

A seven element array arranged in a hexagonal shape, as shown in Fig. 8, is under investigation. Results on radiation pattern, as shown in Fig. 9 to 12, are produced in both linear and circular polarizations. They are obtained with the element separation and the dielectric constant of the substrate as parameters. The array is designed to operate at 0.832GHz and at a substrate depth of 1.59mm (0.00441λ). The pattern is observed at ϕ=0° plane and scanned at θ_0=45° or θ_0=70° and ϕ_0=0°. Those results are by no means to include all the details of the hexagonal array, instead they reflect a general behavior of the array and serve as a design reference. For different design interests, both TM_{11} and TM_{21} are reported.

With each element fed by a single probe, Fig. 9 and 10 illustrate the E-plane pattern in linear polarization. Fig.

11 and 12 give the gain pattern in circular polarization where each array element is fed by two feed placed at $\phi=0^{o}$, and 90^{o} with a 90^{o} phase difference. The pattern of symmetry has verified for the unscanned array. Apparently, the seven element array is capable of producing a gain of more than 10 dB. The following discussion will be on how the element spacing and the dielectric constant of the substrate affect the overall pattern.

Element spacing: The larger the spacing, the lesser the coupling effect. This is verified by varying the element distance from 0.55λ to 0.7λ as shown from Fig. 9 to 12. With a spacing of 0.55λ or beyond, the main beam changes slightly due to mutual coupling. Although mutual coupling often reduces the gain, as shown in Fig. 9 and 11 at a spacing of 0.55λ, it is not so in the case where the spacing is 0.7λ. In fact, the gain of the array is enhanced under the influence of mutual coupling. The ratio between the amplitudes of the grating lobe and the main lobe increases directly with the extension of the spacing. In both polarization cases, scanning the array away from the broadside shifts the main beam and its side lobes towards the endfire direction. In the mean time, the amplitude of the main beam drops drastically with the increase of the scan angle θ_0.

Dielectric constant: The lower the dielectric constant is used, the higher the gain is produced. In addition, the main beam moves towards the broadside as the dielectric constant

decreases. Not much discrepancy can be found between the coupled and the uncoupled patterns at ϵ_r=2.32 and 2.6. Nevertheless, it is apparent that mutual coupling plays an important role for low values of ϵ_r where the gain is much reduced and the grating lobe is incredibly high.

Scanning the beam of the array to $\phi=0^o$, the pattern, as shown in Fig. 13 and 14, are observed at different ϕ-plane. Fig. 13d and 14d provided variations between the gain and the azimuthal angle ($0^o \leq \phi \leq 180^o$). With the beam of the array maximized at $\phi=30^o$ at TM_{11} mode, Table 2 gives a brief account on how the gain(G) and its peak angle(θ) varies with the changing of the element spacing and the excitation angles.

Phase excitation θ_0	Element spacing		
	0.55λ	0.60λ	0.70λ
0^o	G=14.426dB $\theta=0^o$	G=14.902dB $\theta=0^o$	G=15.940dB $\theta=0^o$
30^o	G=13.662dB $\theta=25^o$	G=14.173dB $\theta=25^o$	G=14.780dB $\theta=25^o$
60^o	G=12.036dB $\theta=42^o$	G=11.823dB $\theta=43^o$	G=11.217dB $\theta=45^o$
70^o	G=11.465dB $\theta=45^o$	G=11.052dB $\theta=47^o$	G=10.275dB $\theta=50^o$

TABLE 2

Gain of a progressively phased array, beam at $\phi=30^o$

Those patterns exhibit good and low cross-polarization especially at the main beam position. The maximum cross-polarized component is located at $\theta=90^{0}$. It varies inversely with the element spacing but directly with the scan angle θ_0. Lower the dielectric constant of the substrate reduces the cross-polarized component. As long as the array is not operated at or near the endfire direction, the circular polarization performance of the array is promising.

4.4.2 Bandwidth and return loss

A resonated microstrip patch is usually designed to produce an input impedance to match with the characteristic impedance of the transmission line (standard is 50Ω). It is always desirable to operate the patch at its resonant frequency in order to obtain a maximum power radiation. As a matter of fact, operating the antenna at a non-resonated stage creates an impedance mismatch problem between the antenna and the transmission line. Power reflection occurs and its severeness depends on the extent of the unsuitable match. The reflection coefficient and the return loss are defined as

$$\Gamma = \frac{Z_L - Z_0}{Z_L + Z_0} \tag{4.25}$$

$$L = 20\log_{10}|\Gamma| \tag{4.26}$$

where Z_L is the input impedance of the patch. Numerical results are produced for the first three fundamental modes with a resonant frequency of 0.832GHz. Variations of the operating frequency, the power gain, the input impedance and the return loss are tabulated in Appendix D with the substrate thickness and its dielectric constant as parameters.

If the frequency bandwidth is defined to be the difference of the normalized frequencies which produce the same amount of return loss, the following results are observed:

$$\frac{BW_2}{BW_1} = \sqrt{\frac{\epsilon_{r1}}{\epsilon_{r2}}} \qquad (4.27)$$

$$\frac{BW_2}{BW_1} = \frac{h_2}{h_1} \qquad (4.28)$$

where BW_1 is the bandwidth of the antenna corresponding to its substrate thickness h_1 and permittivity ϵ_{r1}. The same relationship holds for BW_2, h_2, and ϵ_{r2}. The bandwidth can thus be increased by decreasing the substrate permittivity or increasing its thickness.

4.5 SUMMARY

Based on a cavity modal-expansion model, the induced electric and magnetic sources are expressed in terms of the hypothetical magnetic and electric components, respectively. They are used to calculate the corresponding vector potentials where these potentials are responsible for deriving

the far field pattern. The total radiated power by the array can be evaluated by performing a surface integration of the surface current around the radiating aperture. It can also be found by integrating over the upper hemispheric surface with respect to the poynting vector. Both results agree to each other very closely. Expressions of the gain on linear and circular polarizations are established. Finally, some results on the gain pattern of a seven element array are presented. Mutual coupling does not affect the overall pattern significantly when the element spacing is 0.55λ or beyond. Gain is not always degenerated by the mutual coupling, but enhanced sometimes. Increasing the spacing also increases the grating lobe relatively. The array gives a good circular polarization pattern except at the endfire direction ($\theta=90^{o}$) where the maximum cross-polarized component occurs. Increasing the substrate thickness or decreasing the dielectric constant would improve the bandwidth of the microstrip antenna.

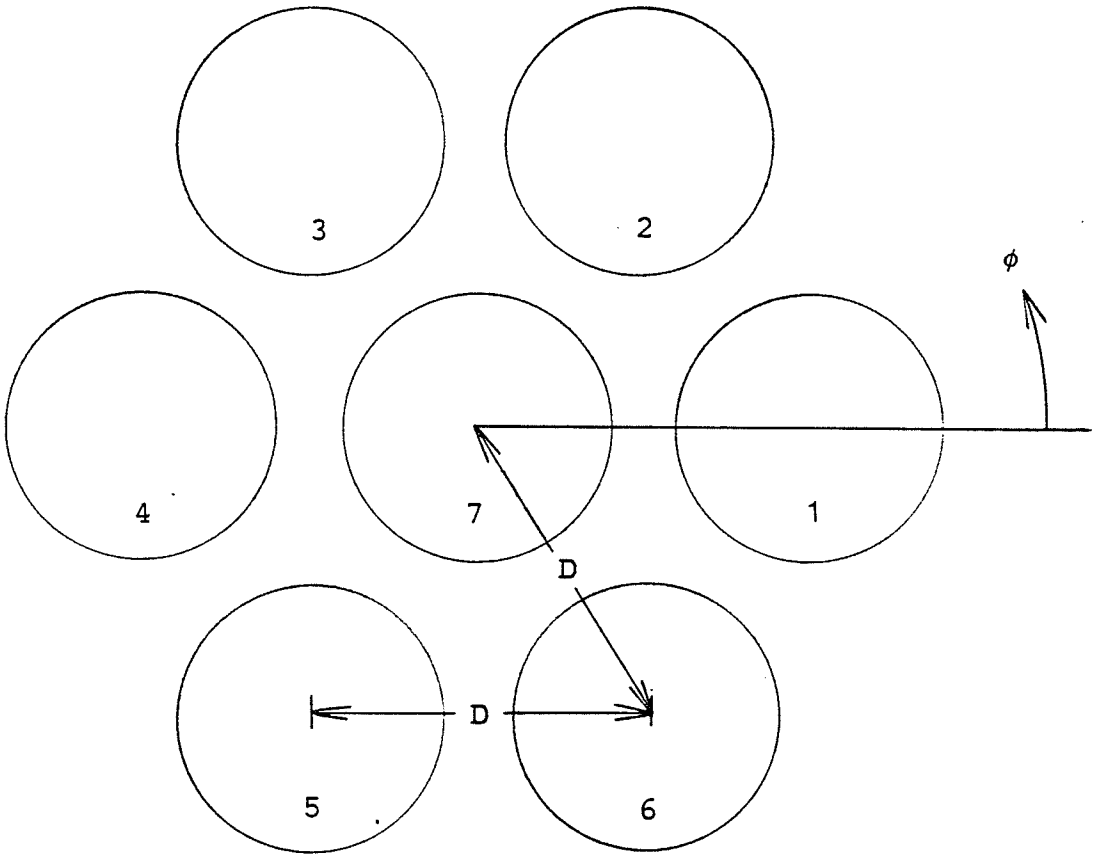

Figure 8: A seven element array in hexgonal shape

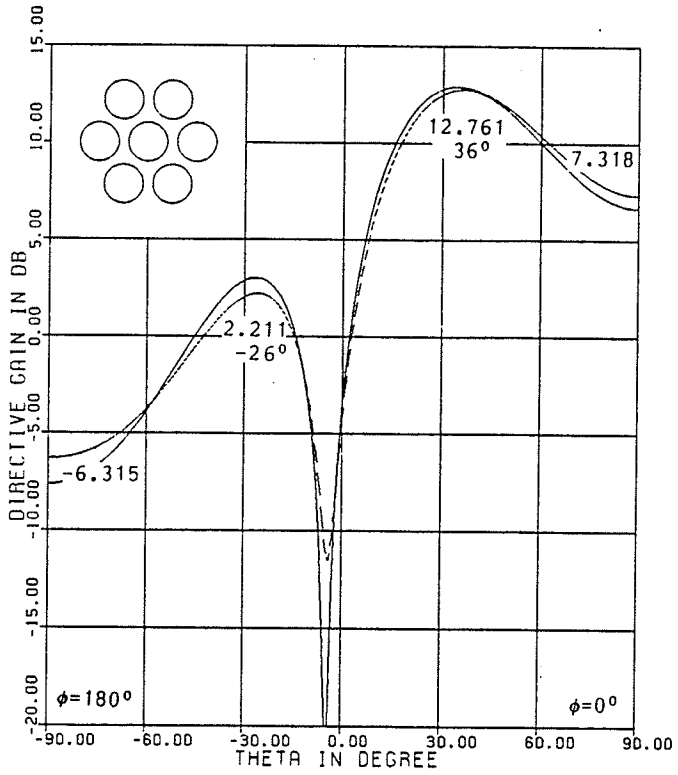

(a) ϵ_r=2.32, θ_0=45°, ϕ_0=0°, D=0.55λ

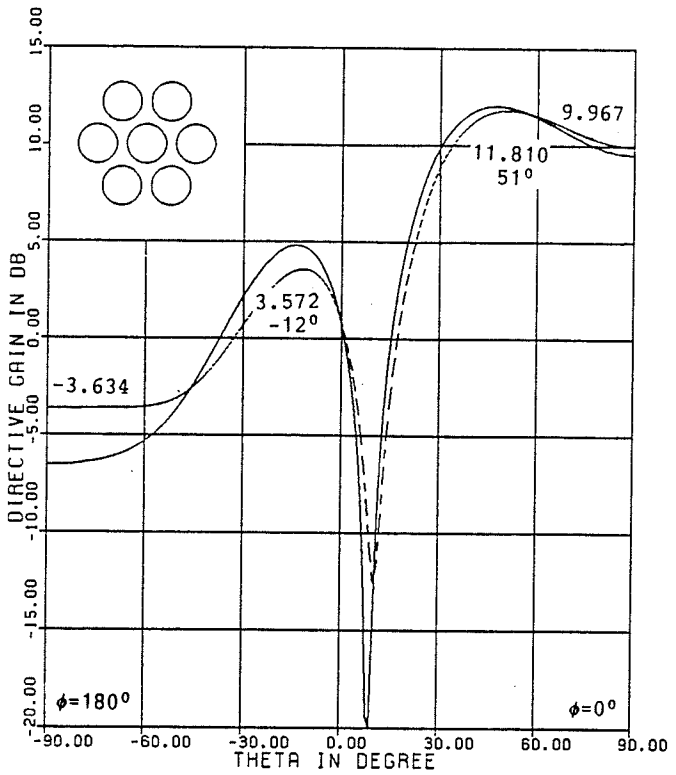

(b) ϵ_r=2.32, θ_0=70°, ϕ_0=0°, D=0.55λ

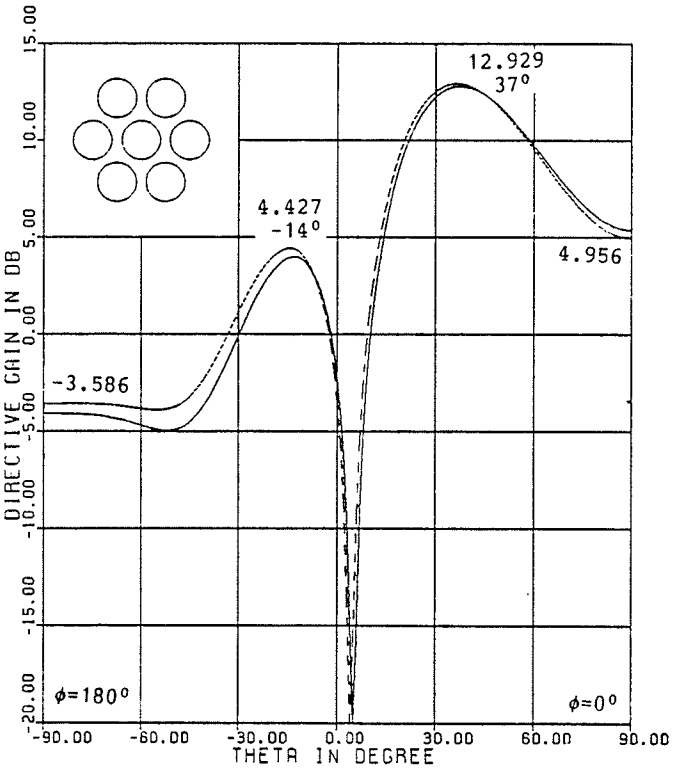

(c) ϵ_r=2.32, θ_0=45°, ϕ_0=0°, D=0.70λ

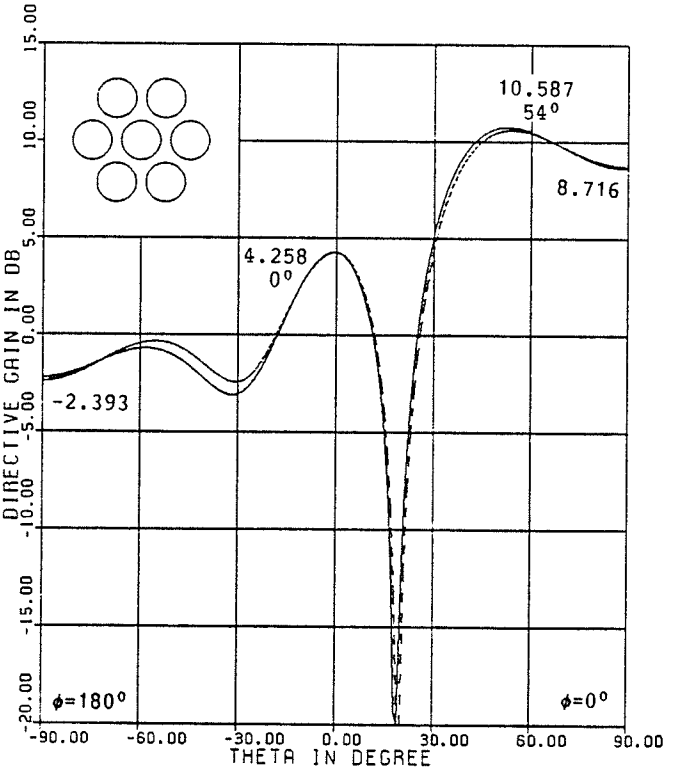

(d) ϵ_r=2.32, θ_0=70°, ϕ_0=0°, D=0.70λ

Figure 9: E-plane pattern of TM_{11} mode
--- coupling, —— no coupling

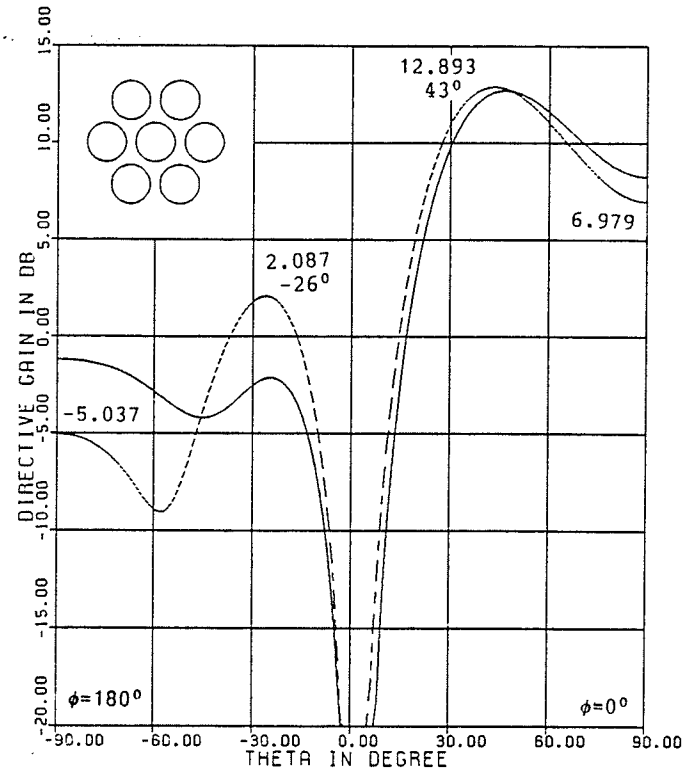

(a) ϵ_r =2.32, θ_0=45°, ϕ_0=0°, D=0.70λ

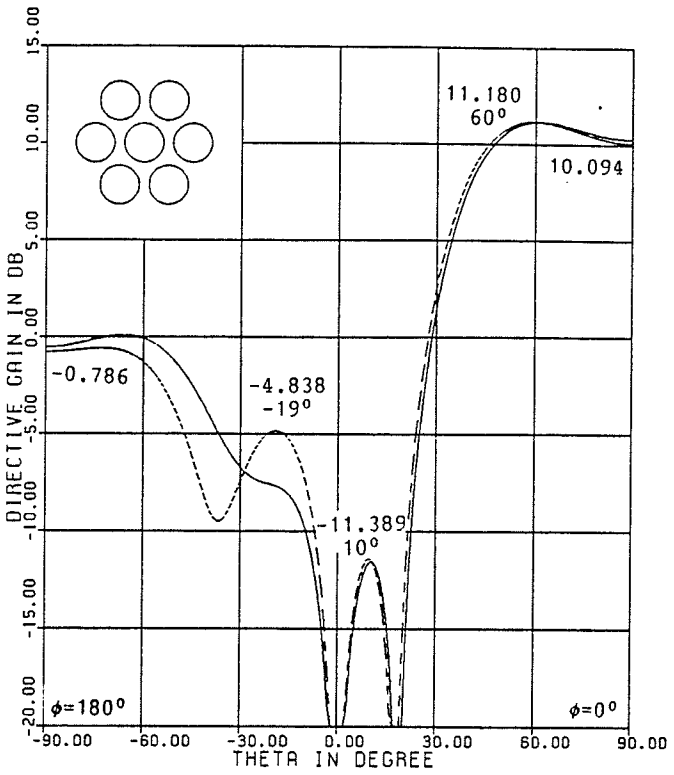

(b) ϵ_r =2.32, θ_0=70°, ϕ_0=0°, D=0.70λ

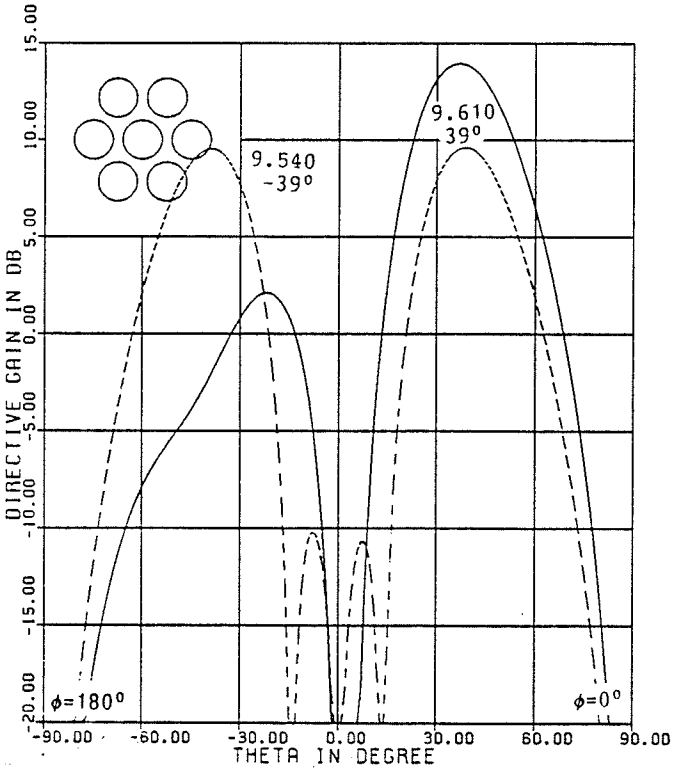

(c) ϵ_r =1.0, θ_0=45°, ϕ_0=0°, D=0.70λ

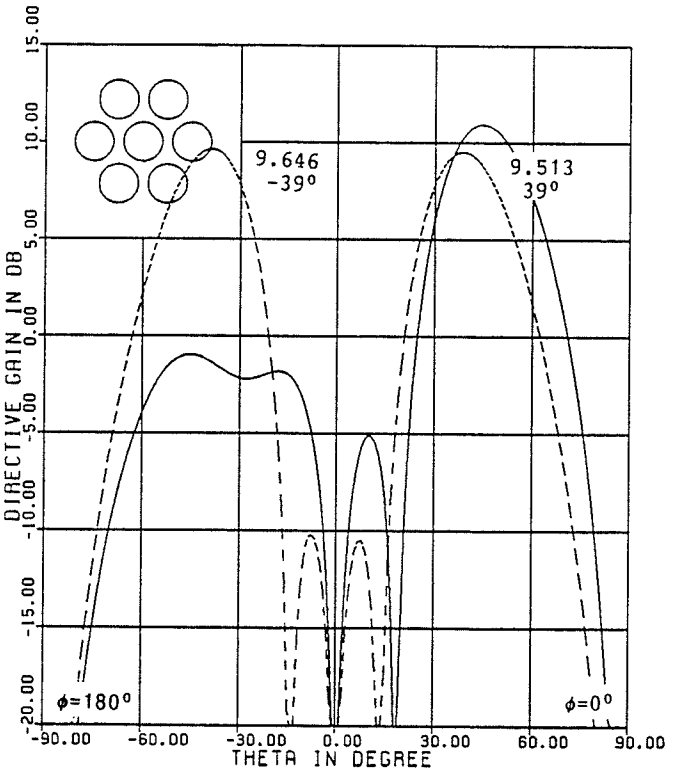

(d) ϵ_r =1.0, θ_0=70°, ϕ_0=0°, D=0.70λ

Figure 10: E-plane pattern of TM_{21} mode
--- coupling, —— no coupling

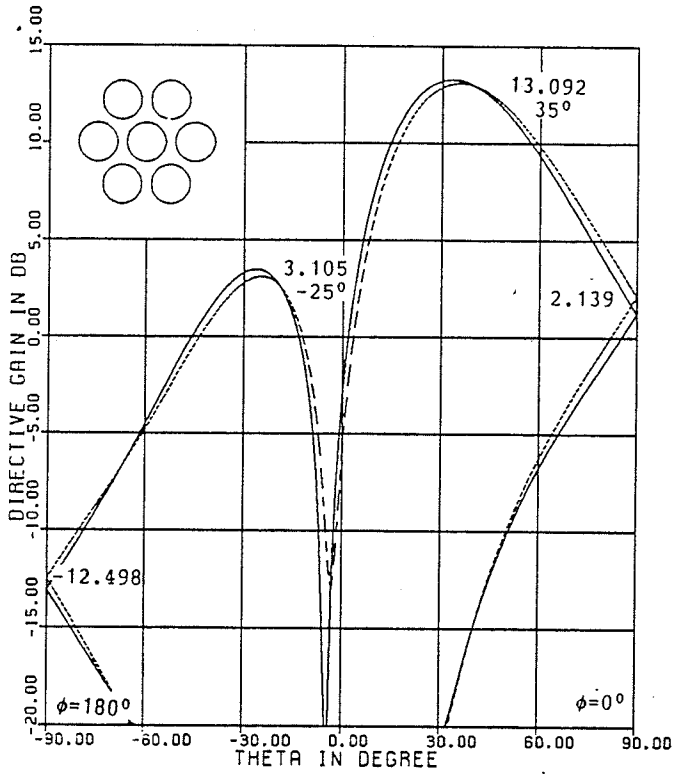

(a) ϵ_r=2.32, θ_0=45°, ϕ_0=0°, D=0.55λ

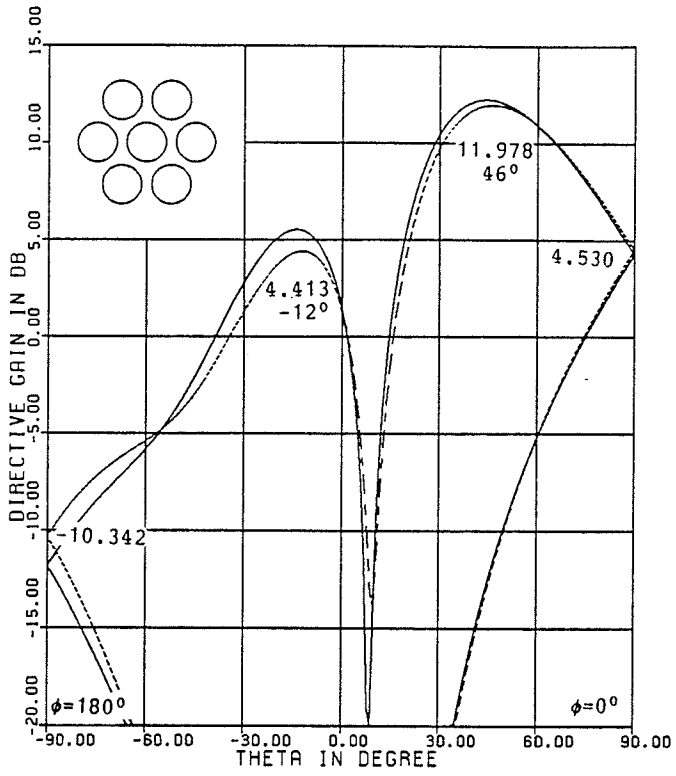

(b) ϵ_r=2.32, θ_0=70°, ϕ_0=0°, D=0.55λ

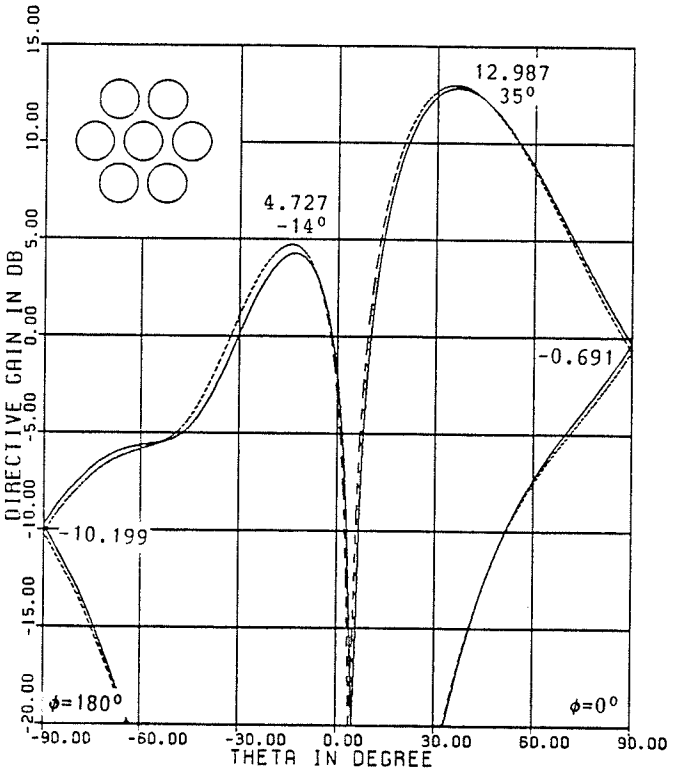

(c) ϵ_r=2.32, θ_0=45°, ϕ_0=0°, D=0.70λ

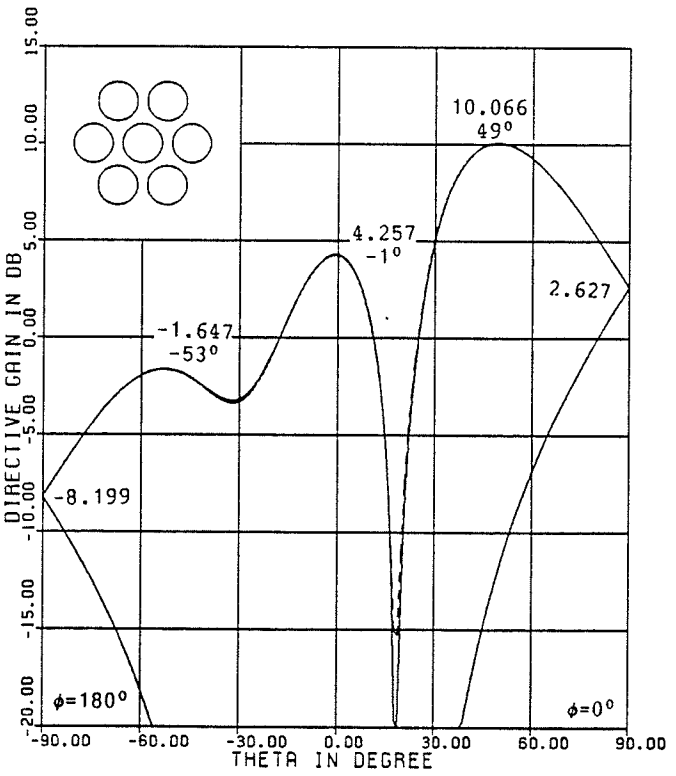

(d) ϵ_r=2.32, θ_0=70°, ϕ_0=0°, D=0.70λ

Figure 11: Radiation pattern (TM_{11} mode) in circular polarization, --- coupling, —— no coupling

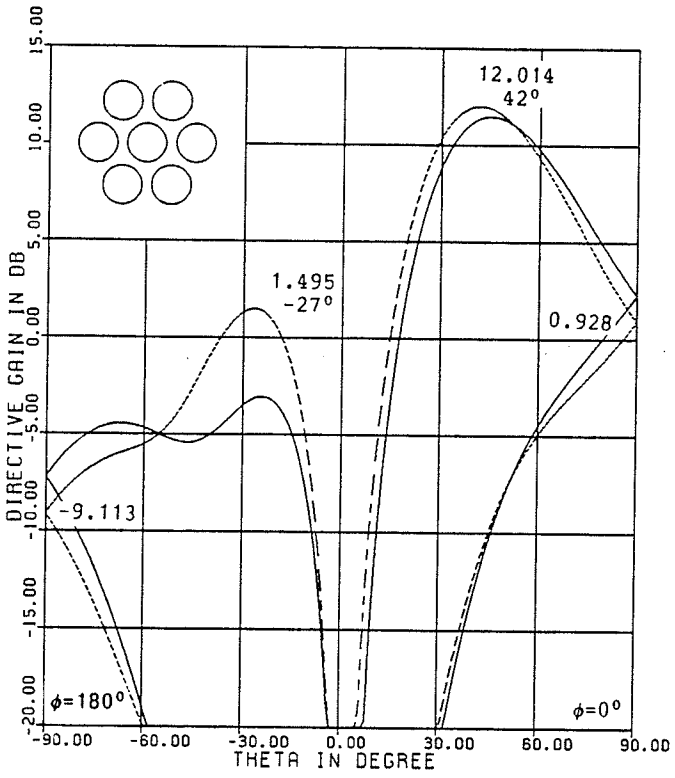

(a) $\epsilon_r = 2.6$, $\theta_0 = 45°$, $\phi_0 = 0°$, D=0.70λ

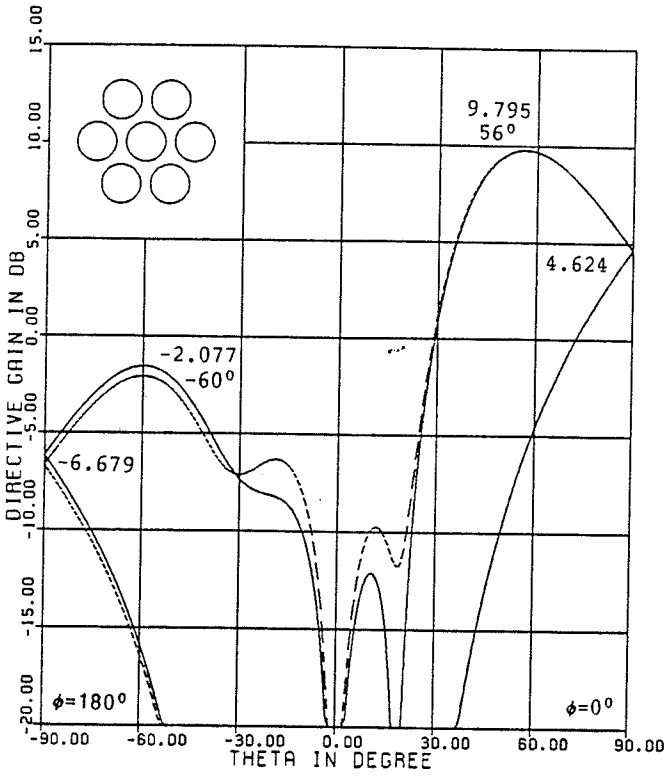

(b) $\epsilon_r = 2.6$, $\theta_0 = 70°$, $\phi_0 = 0°$, D=0.70λ

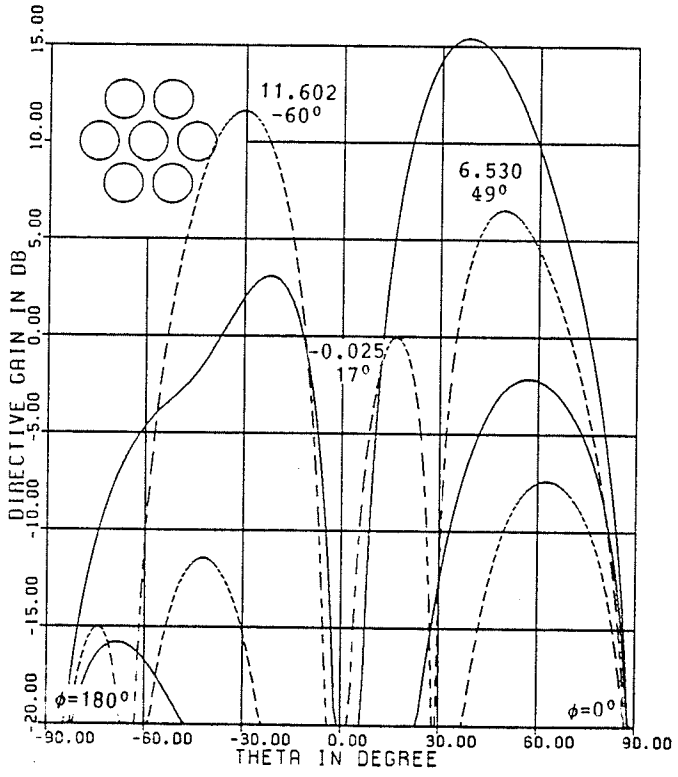

(c) $\epsilon_r = 1.0$, $\theta_0 = 45°$, $\phi_0 = 0°$, D=0.70λ

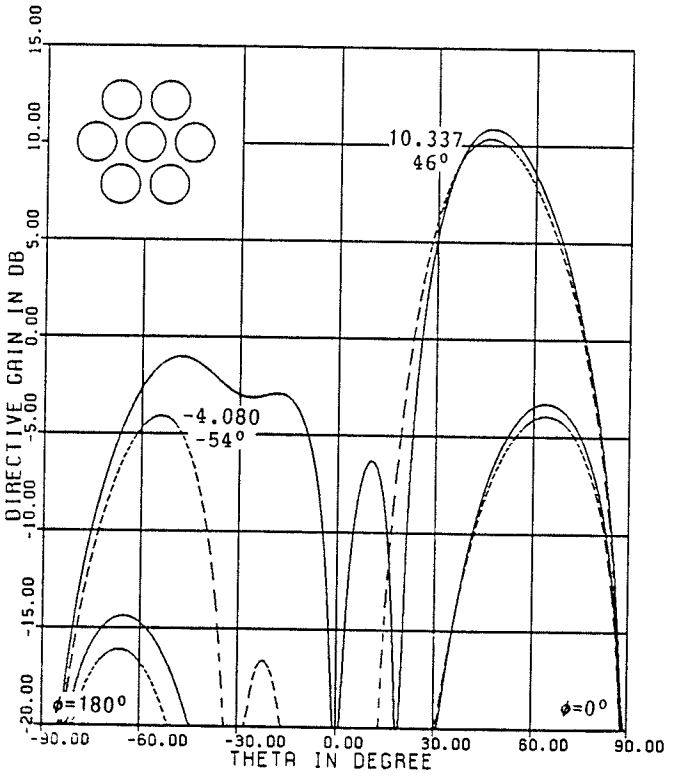

(d) $\epsilon_r = 1.0$, $\theta_0 = 70°$, $\phi_0 = 0°$, D=0.70λ

Figure 12: Radiation pattern (TM_{21} mode) in circular polarization, --- coupling, —— no coupling

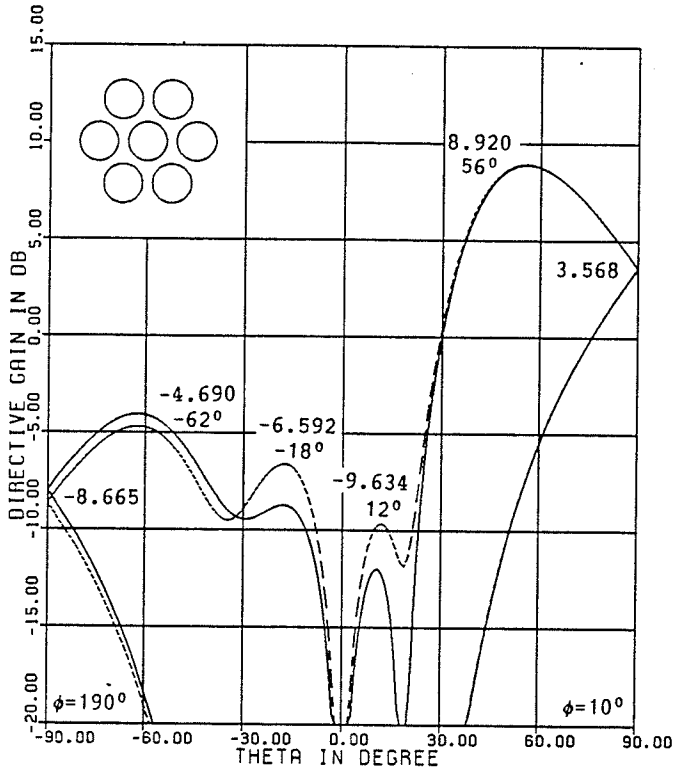

(a) Plane at ϕ=10°, θ_0=70°

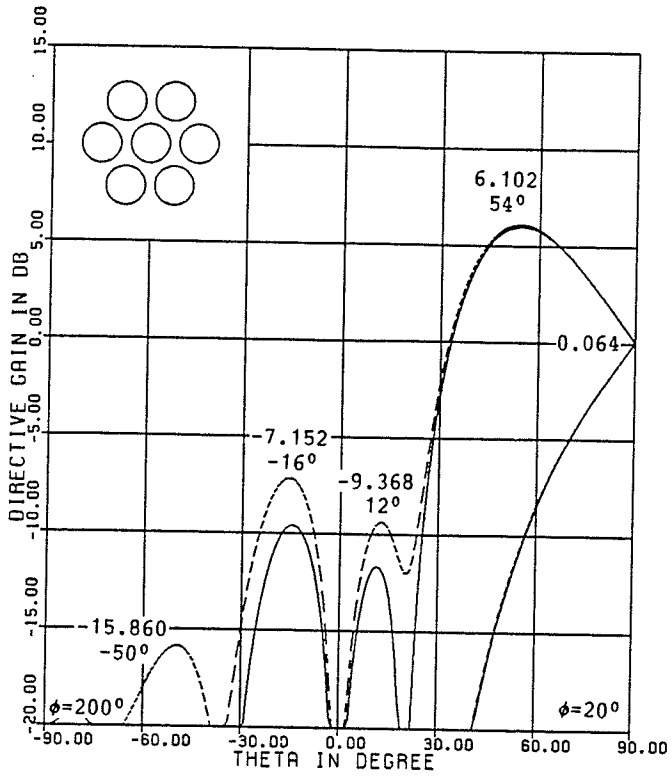

(b) Plane at ϕ=20°, θ_0=70°

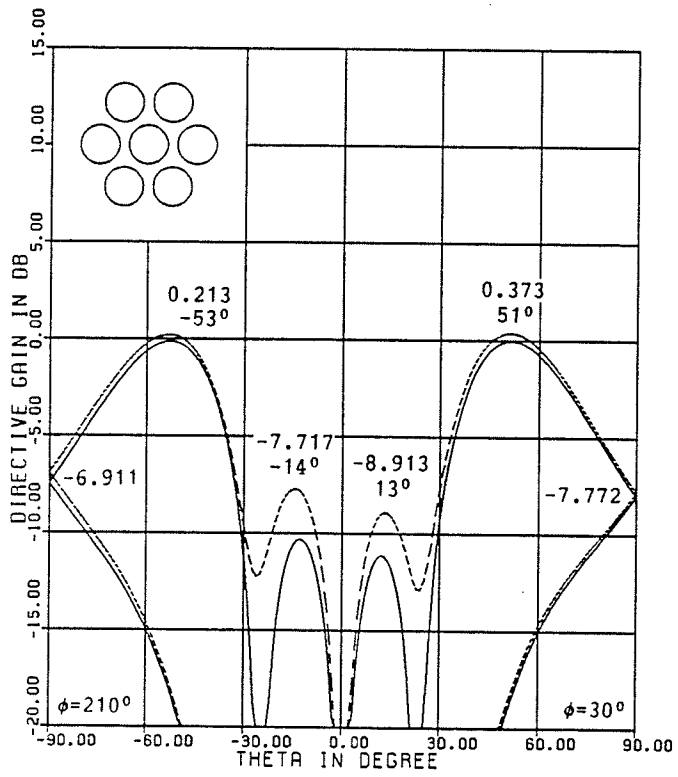

(c) Plane at ϕ=30°, θ_0=70°

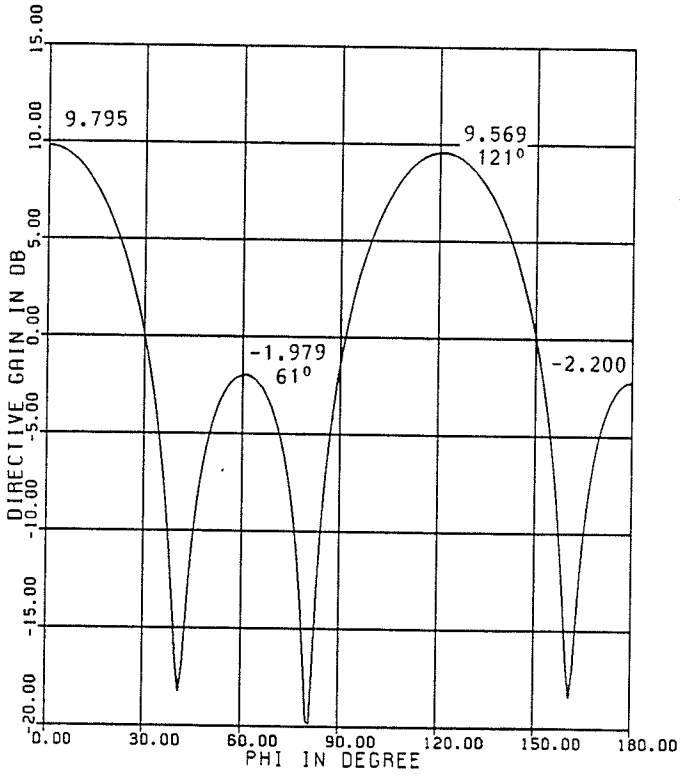

(d) ϕ-plane pattern, θ_0=70°

Figure 13: ϕ-plane pattern (TM_{21} mode) with ϵ_r=2.6, element spacing=0.7λ, array beam at 0°
--- coupling, —— no coupling

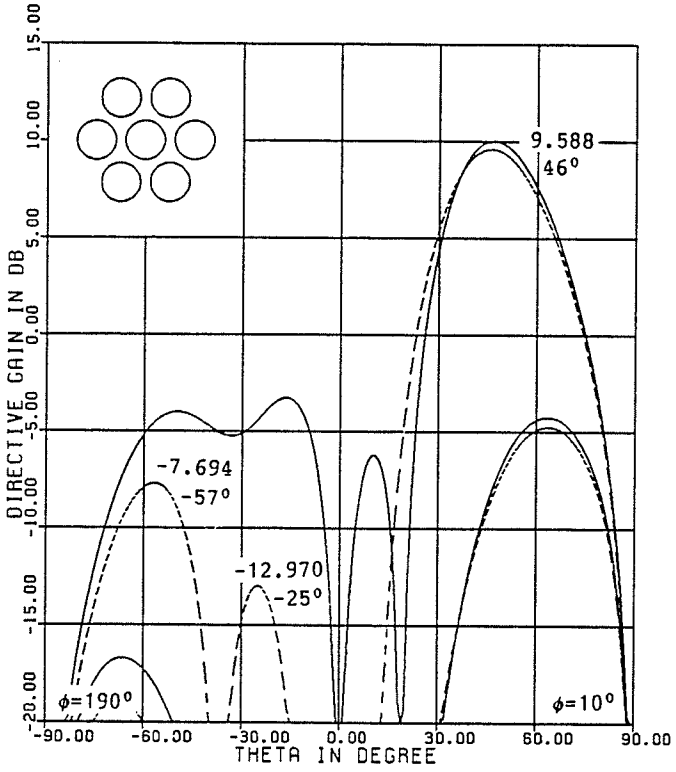

(a) Plane at $\phi=10^{\circ}$, $\theta_0=70^{\circ}$

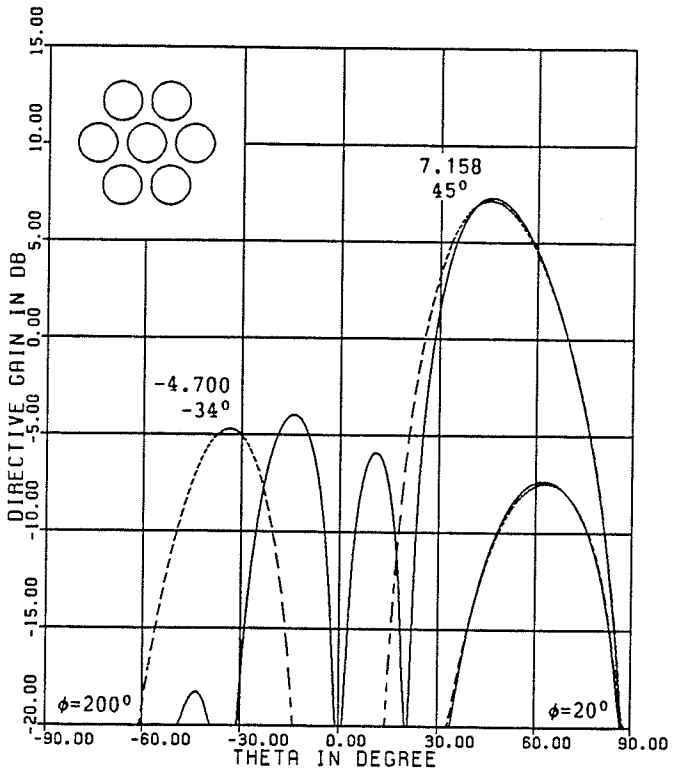

(b) Plane at $\phi=20^{\circ}$, $\theta_0=70^{\circ}$

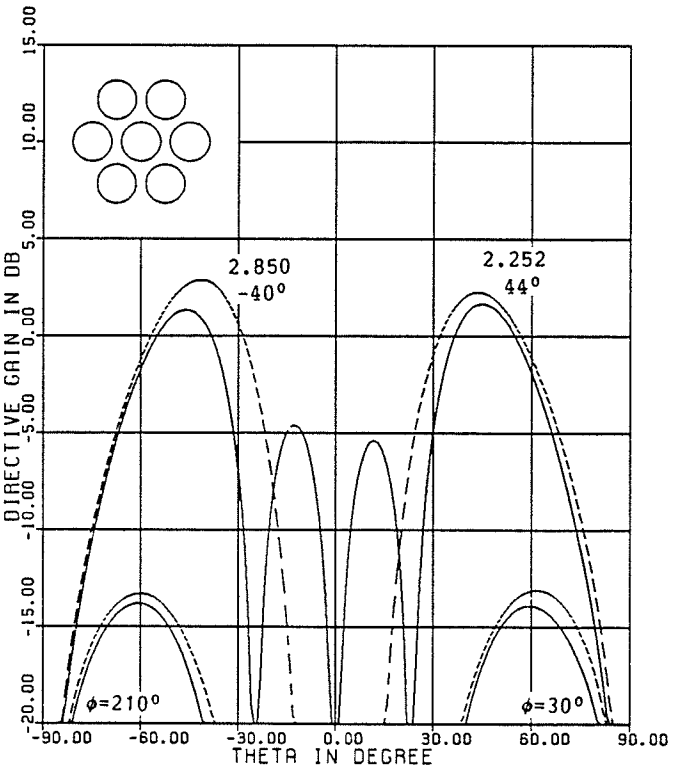

(c) Plane at $\phi=30^{\circ}$, $\theta_0=70^{\circ}$

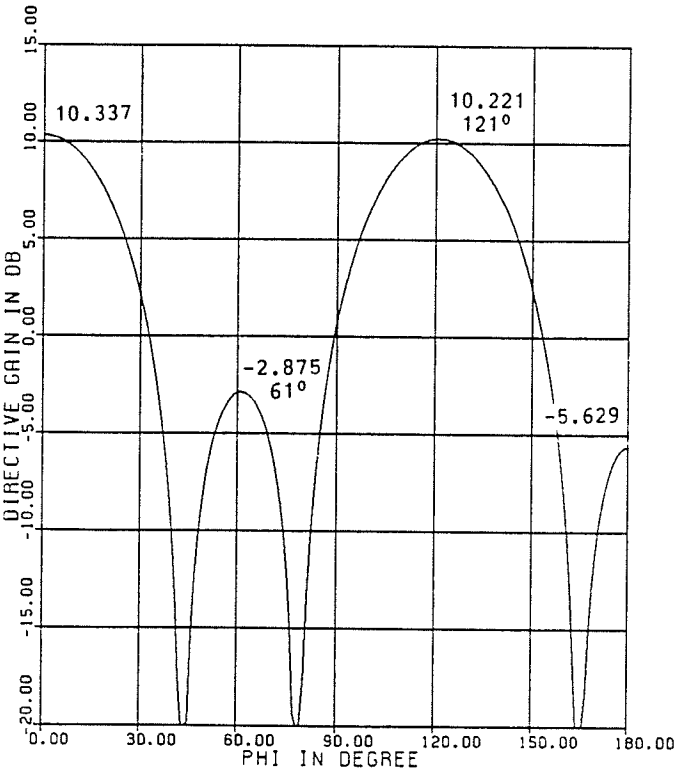

(d) ϕ-plane pattern, $\theta_0=70^{\circ}$

Figure 14: ϕ-plane pattern (TM_{21} mode) with $\epsilon_r=1.0$, element spacing=0.7λ, array beam at 0°
--- coupling, —— no coupling

Chapter V

MULTILAYER MICROSTRIP ANTENNA

5.1 INTRODUCTION

Despite those distinct advantages such as thin profile, compactness, and low cost that microstrip antenna possesses, shortcomings including limited bandwidth, low gain, and poor efficiency have created problems for investigators to strive for improvement. Various microstrip structures are proposed and deployed according to various specific applications and performance. Among them, multilayer microstrip antenna is one of the recent developed technique. It has been found that by stacking layers of microstrip disc with dielectric substrate in between as support can increase the bandwidth range [27]. Since the disc of different levels resonate at different frequency, the stacked structure can be utilized for multiple frequency application [28] where the operation of two or more discrete bands is required. In this chapter, the stacked elements are designed to response at a particular frequency but in different resonant modes. The total radiated power of a single multi-layer microstrip is derived for normalization purpose. A two-layer stacked microstrip, operated at TM_{11} and TM_{21} modes, is studied thoroughly. A linear vertical array and a planar array of the stacked microstrip are discussed and cited as examples.

5.2 POWER CALCULATIONS

For a multi-layered microstrip antenna, the upper element radiates with respect to its counterpart at a lower level as its ground plane. The effect of those finite ground plane are assumed to be minimal. Each disc radiates independently and coupling between different apertures is neglected. Consider a stacked microstrip antenna with n layers, the total radiated power generated by the antenna can be calculated by taking a closed surface integral over the poynting vector and is given by

$$P_t = \frac{1}{2} \oint_s (\bar{E} \times \bar{H}^*) \cdot \bar{ds} \tag{5.1}$$

where

$$\bar{E} = \sum_{i=1}^{n} (\bar{\theta}\, E_\theta^i + \bar{\phi}\, E_\phi^i) \tag{5.2a}$$

$$\bar{H} = \sum_{i=1}^{n} (\bar{\theta}\, H_\theta^i + \bar{\phi}\, H_\phi^i) \tag{5.2b}$$

and $\bar{ds} = \bar{r} r^2 \sin\theta d\theta d\phi$. E_θ^i, E_ϕ^i, H_θ^i, and H_ϕ^i are the electric and magnetic field components generated by the i-th layer of the n layered microstrip antenna. The superscript * is the conjugate value of the referred field parameter. In terms of the intrinsic impedance of free space, the electric and magnetic components can be expressed as

$$E_\theta^i = \eta_o H_\phi^i \tag{5.3a}$$

$$E_\phi^i = -\eta_o H_\theta^i \tag{5.3b}$$

Substituting equation 5.2 and 5.3 into 5.1, the total radiated power can be obtained as

$$P_t = \frac{1}{2\eta_0} \int \{ |\sum_{i=1}^{n} E_\theta^i|^2 + |\sum_{i=1}^{n} E_\phi^i|^2 \} \, ds \qquad (5.4)$$

Equation 5.4 is used as a power normalization factor in the gain pattern calculation. It can be generalized to the stacked microstrip array with the array factor incorporated into the electric components.

5.3 TWO-LAYER STACKED MICROSTRIP ANTENNA

For a fixed operating frequency, the patch radius varies directly with its resonant mode. The higher the resonant mode, the larger the patch radius. It is necessary to place the small patch on top of the large patch to ensure that a ground plane is always available with respect to the upper patch and also eliminates the obstruction of the radiating waves due to the patch.

A fundamental approach to the stacked microstrip antenna starts with a two-layered structure. It is designed to resonate at TM_{11} and TM_{21} modes. Each patch is fed by a coaxial cable with a pre-calculated feed location for impedance matching. Since the substrate thickness is much smaller than the wavelength, the outgoing waves are assumed to be in phase. Alternatives can be made on the magnitude selection

of the two voltage feeds which in turn controls the radiation pattern of the stacked structure. It is because of the combination that a scanning effect, as shown in Fig. 15 recorded at $\phi=90^0$ plane, is produced. Keeping the excitation of the TM_{11} mode as unity (Fig. 15a and 15b), raising the TM_{21} voltage steepens the main beam and lowers the side lobe. Increasing the TM_{11} voltage but leaving the TM_{21} voltage at its extremum (Fig. 15c and 15d), however, enhances the main beam and reduces the side lobe. It is found that a ratio of 1:0.9 between the TM_{11} and TM_{21} modes gives the best pattern composed of a relatively sharp main beam and low side lobe. A maximum gain is located at $\phi=90^0$ plane with a gain of 7.797dB at $\theta=-31^0$ ($\theta=31^0$ if observed at $\phi=270^0$ plane). It is an increase of 0.55 dB over a single patch operated at TM_{11} mode. Maximum cross-polarization level occurs at $\theta=-90^0$ at $\phi=270^0$ with a magnitude of -0.527dB.

Due to the operation of mixed resonant modes (TM_{11} and TM_{21}), the overall radiation pattern of the structure is ϕ-dependent. Fig. 16 illustrating the ϕ-dependence of a stacked antenna by observing the pattern at different ϕ-plane with unity voltages on both feed. The gain shrinks along the ϕ-direction when the observation plane moves away from the $\phi=270^0$ plane.

In practice, an identical patch, not connected by any feed, is placed on top of the radiating patch leaving an air-gap of depth H in between in order to increase the band-

width. The insertion of the air-gap deteriorates the pattern because the wave radiated from the aperture cannot be assumed in phase. The degree of distortion depends on the size of the gap. Fig. 17a to 17c indicate the variations between the radiation pattern and the air-gap when the gap size varies from 0.05λ to 0.15λ. The pattern formulations including the air-gap are given by

$$E_\theta = E_\theta^{21} + E_\theta^{11}\, e^{jk_0 H\cos\theta} \tag{5.5a}$$

$$E_\phi = E_\phi^{21} + E_\phi^{11}\, e^{jk_0 H\cos\theta} \tag{5.5b}$$

where E_θ^{11}, E_ϕ^{11}, and E_θ^{21}, E_ϕ^{21} are the radiated far fields of the TM_{11} and TM_{21} elements, respectively. They are defined in equation 4.7 and 4.8. Remedy can be made by feeding the top patch, responsible for TM_{11} mode, with a phase difference of θ' relative to the feed of the lower patch where θ' is defined as

$$\theta' = k_0 H\cos\theta_p \tag{5.6}$$

where $k_0(=2\pi/\lambda)$ is the free space wavelength, θ_p is the peak angle of the main beam with no air-gap and θ' is in radian. With $H=0.1\lambda$ and $\theta_p=32^0$, an example is shown in Fig. 17d where the phase of the TM_{11} wave is corrected and added with the TM_{21} wave coherently. The improvement is obvious when comparing Fig. 17b and 17d with 16c.

Similarly, a multi-layer stacked microstrip antenna can be constructed and operated according to the same analogy. Fig. 18 demonstrating the results of some of the multi-layer stacked microstrip. It shows that the gain rises with the increase of stacked elements. Besides, the pattern is somehow predictable. Pattern similarities can be observed between Fig. 18a and 18c due to the odd number of combined resonant modes in consecutive order. Resemblance with regard to the even number of patches can be found between Fig. 16c and 18b. Fig. 18d illustrates another pattern when the feed voltages are altered with respect to Fig. 18c. In fact, many novel patterns can be obtained by having different numbers of stack and various combinations of their feed voltages provided that a possible upward extension by the antenna does not impose any serious threat on the whole operation.

5.4 STACKED MICROSTRIP ARRAY

Knowing the properties of a stacked microstrip of multi-layer, it becomes straight forward to have it applied to stacked microstrip array. A linear vertical array and a two dimensional array of stacked microstrips will be presented.

5.4.1 Linear vertical array

Stacked microstrip elements are placed along the z-axis, perpendicular to the patch with a separation of D, to form a linear vertical array. For simplicity, mutual coupling be-

tween different radiating apertures is not included. In fact, the coupling effect does not cause much problem on the overall pattern, as shown previously, when ϵ_r=2.32. In addition, the coupling between a vertical array is much less than that of a horizontal array in practical cases.

The total radiation pattern is again the product of the element pattern and the array factor of the vertical array. The element pattern is the same as those in equation 5.5. A phase correction expression is used as the array factor and is given by

$$AF(\theta) = \sum_{i=1}^{n} e^{jk_0(i-1)D\cos\theta} \tag{5.7}$$

where n is the total number of array elements, k_0 is the free space wavenumber. Patterns of two and three two-layered (TM_{11} and TM_{21}) microstrip arrays, resonates at 0.832GHz, are shown in Fig. 19 with element spacing of 0.5λ and 0.58λ at ϵ_r=2.32. According to Fig. 19, no increase in gain from the array when compared with a two-layer stacked microstrip, but a power drop of about 2dB on the main beam instead. The main beam is somehow shaped due to the array formation, but the high side lobe, as shown in Fig. 19c and 19d, might create serious problems.

5.4.2 Two dimensional array

A seven two-layer stacked microstrip planar array in hexagonal shape is studied. Again the stacked element is a combination of TM_{11} and TM_{21} modes. Mutual coupling is included between radiating apertures of like modes. Coupling between unlike modes is found to be very small and can be neglected. With ϵ_r=2.32 and operating frequency of 0.832 GHz, Fig. 20 shows the gain pattern of the array with element spacing of 0.65λ and 0.7λ. It is found that for a scan angle θ_0 =70°, a maximum gain is located at ϕ=270° plane. ϕ_0 is thus adjusted to 270° in order to preserve the pattern. Putting a phase difference of 30° in the feed of the TM_{21} patch shifts the observation plane to ϕ=240° as shown in Fig. 20b and 20d. A 3 dB power drop along the ϕ-direction is observed by moving the observation plane by about ±20° in the 0.65λ spacing. Less than 20° is required for the same amount of drop for a spacing of 0.7λ. The larger the element spacing, the sharper the beamwidth around the ϕ-direction or the beam is more shaped. Comparing Fig. 20a and 20c with Fig. 11d and 12b, a gain improvement of more than 3 dB is found in the stacked arrangement except that it varies with the ϕ-angle sensitively.

5.5 SUMMARY

Microstrip antenna in a stacked structure can be used to enhance the gain and improve the pattern. The total power from the stacked antenna is first formulated. Because of a mixed mode operation, the overall pattern is ϕ-dependent. Using different combinations of feed voltage for different level patches creates a scanning effect. The phase correction with the insertion of air-gap is investigated. Mutual coupling between apertures of different modes or different plane levels are assumed to be insignificant. A linear vertical array of stacked microstrip, in general, does not improve the gain but shapes the main beam and raises the side lobe. Finally, a seven element two-layer stacked microstrip planar array is investigated and found to give about 3 dB more in gain than the single layered array. Nevertheless, this extra gain is at the expense of the complexity of the structure, higher material cost and height. Feeding of the array elements is also more difficult to incorporate.

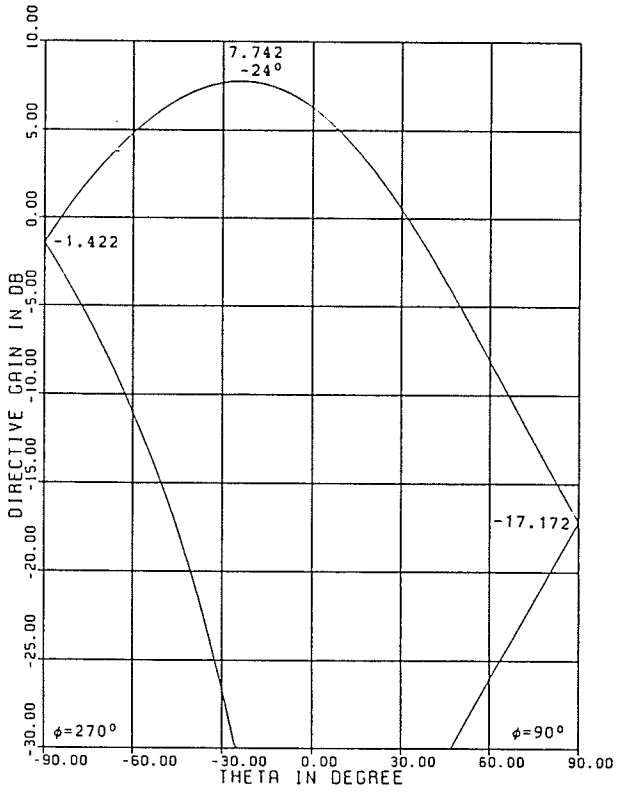

(a) ϵ_r =2.32, V_{11}=1.0, V_{21}=0.5

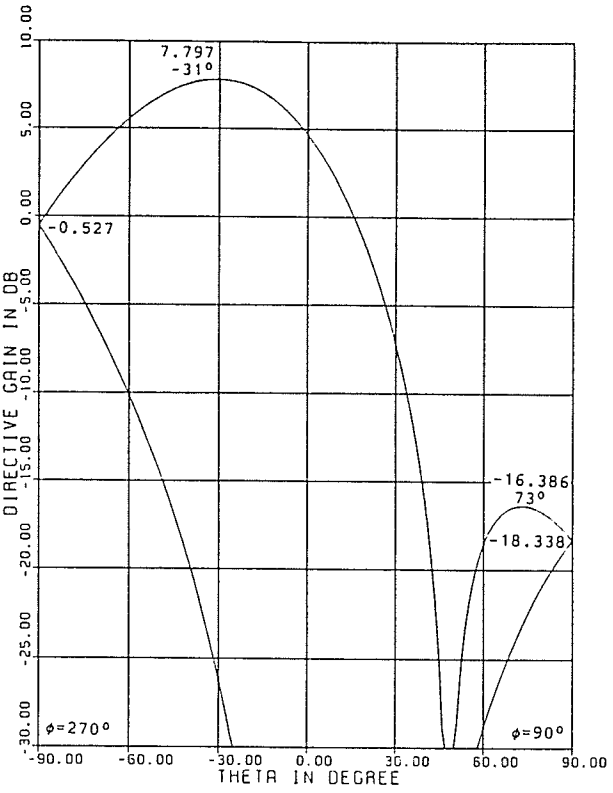

(b) ϵ_r =2.32, V_{11}=1.0, V_{21}=0.9

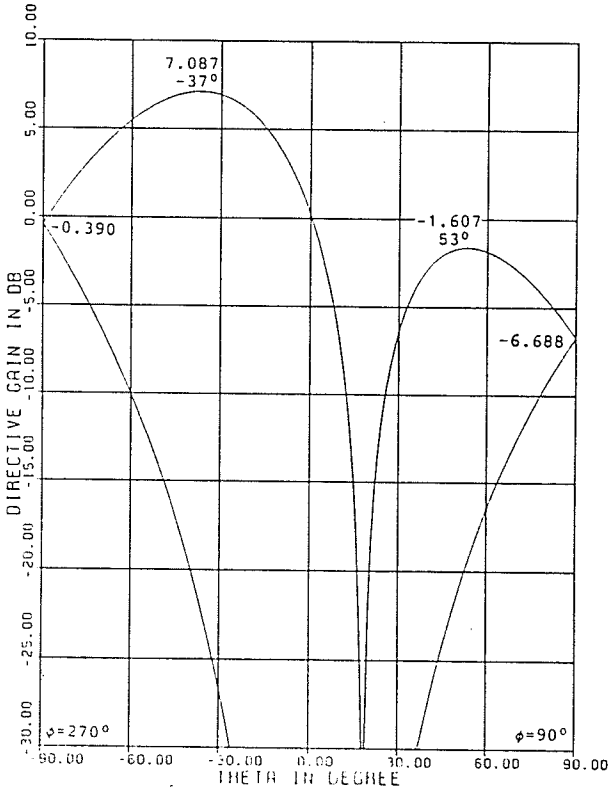

(c) ϵ_r =2.32, V_{11}=0.5, V_{21}=1.0

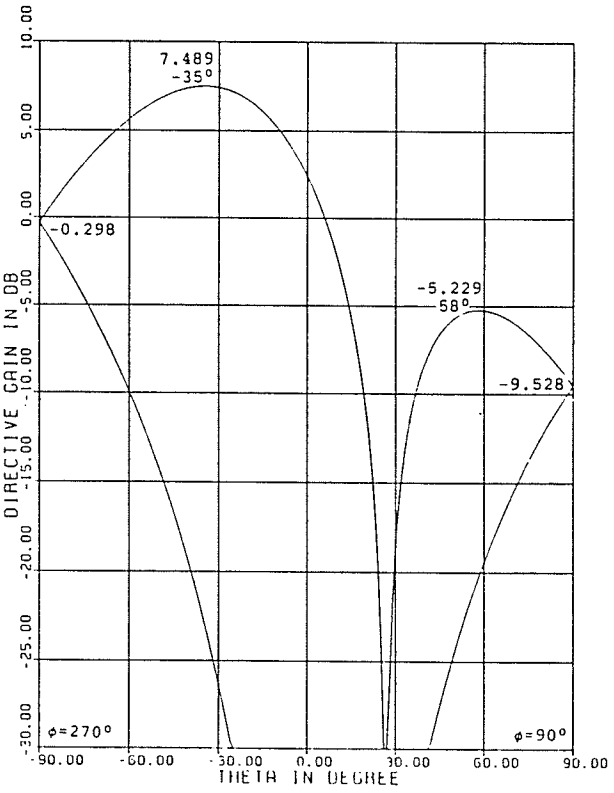

(d) ϵ_r =2.32, V_{11}=0.7, V_{21}=1.0

Figure 15: Pattern of a two layer stacked microstrip antenna (TM_{11} & TM_{21}) with different feed voltages

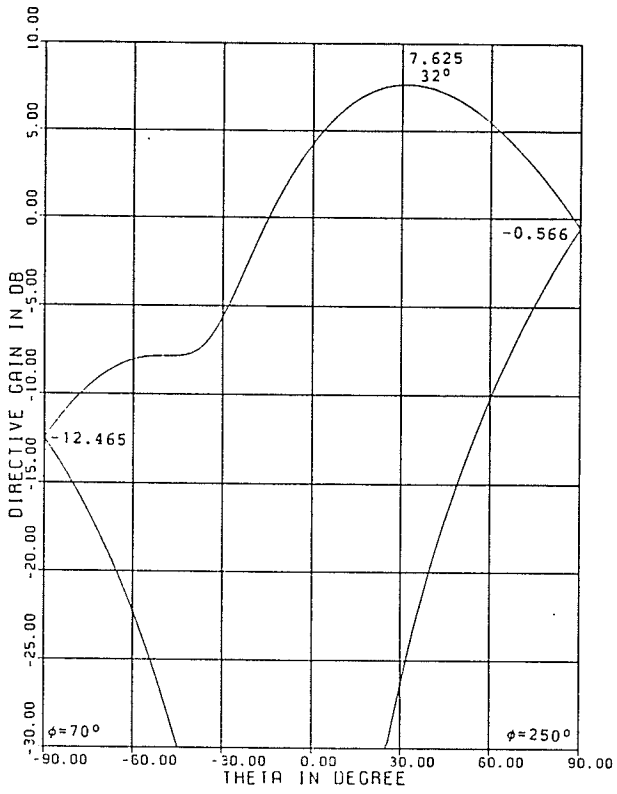

(a) Plane at ϕ=250°

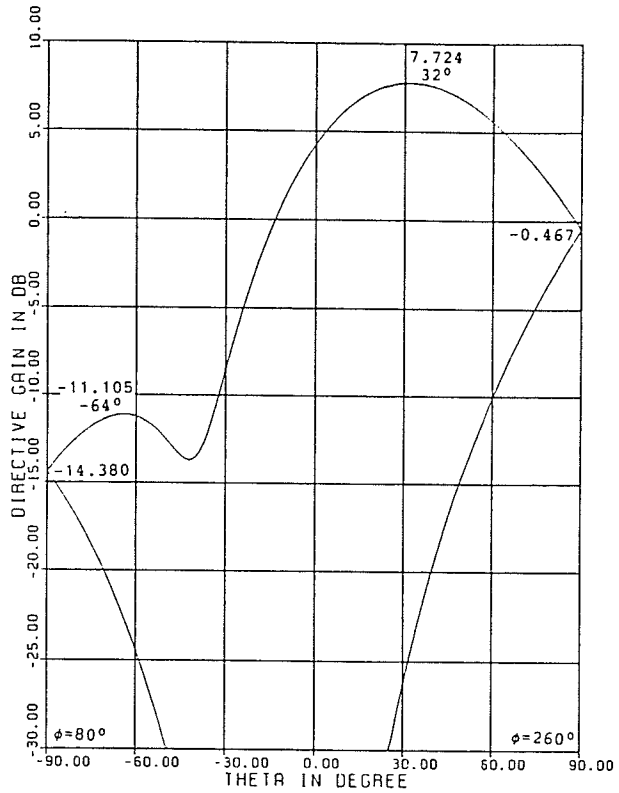

(b) Plane at ϕ=260°

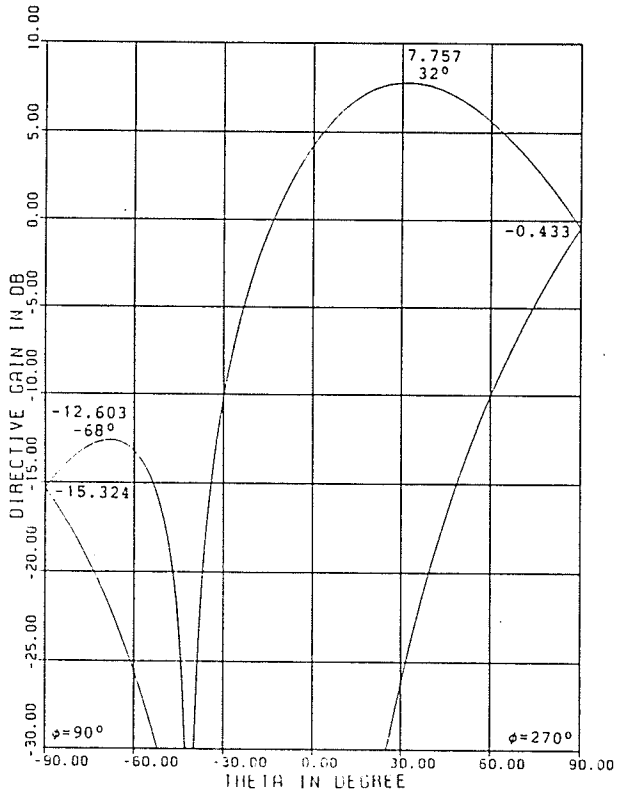

(c) Plane at ϕ=270°

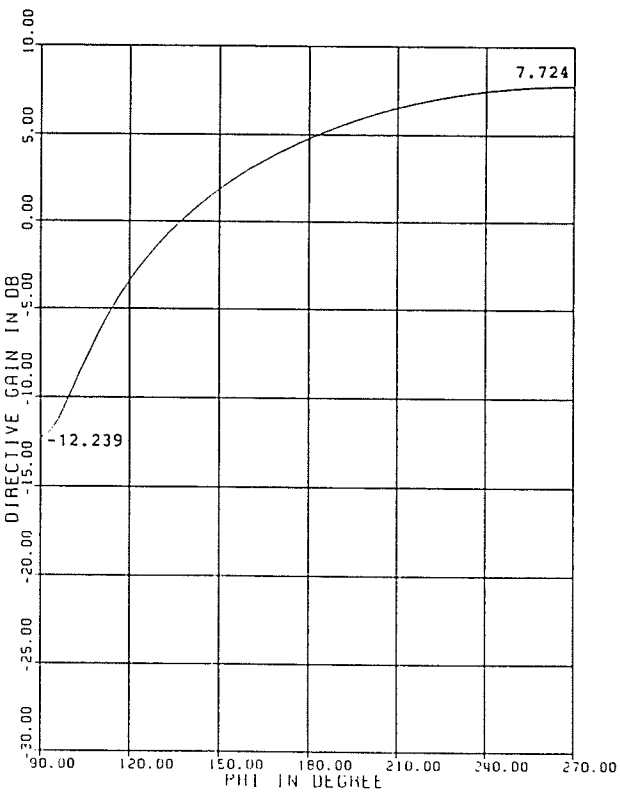

(d) ϕ-pattern

Figure 16: ϕ-plane pattern of a two layer stacked microstrip antenna, ϵ_r=2.32, V_{11}=V_{21}=1.0

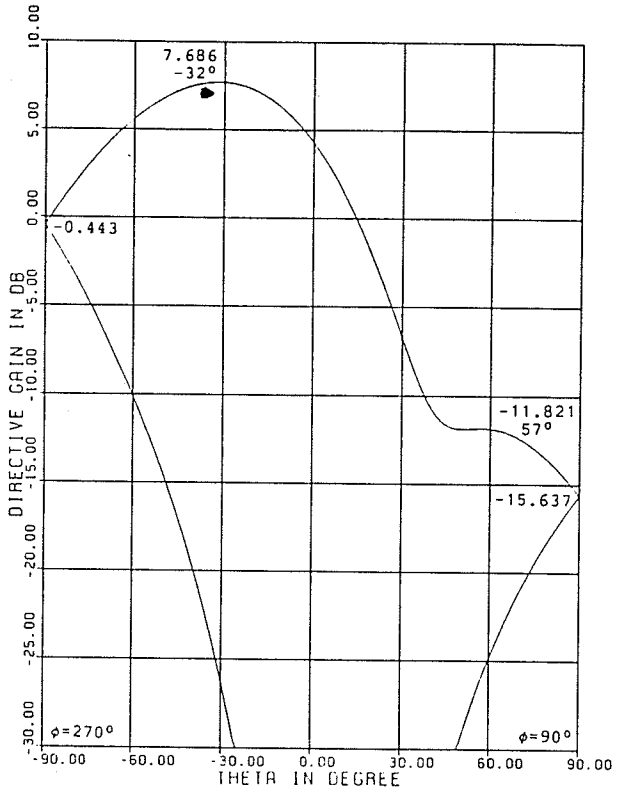

(a) H=0.05λ, $V_{11}=V_{21}=1.0$

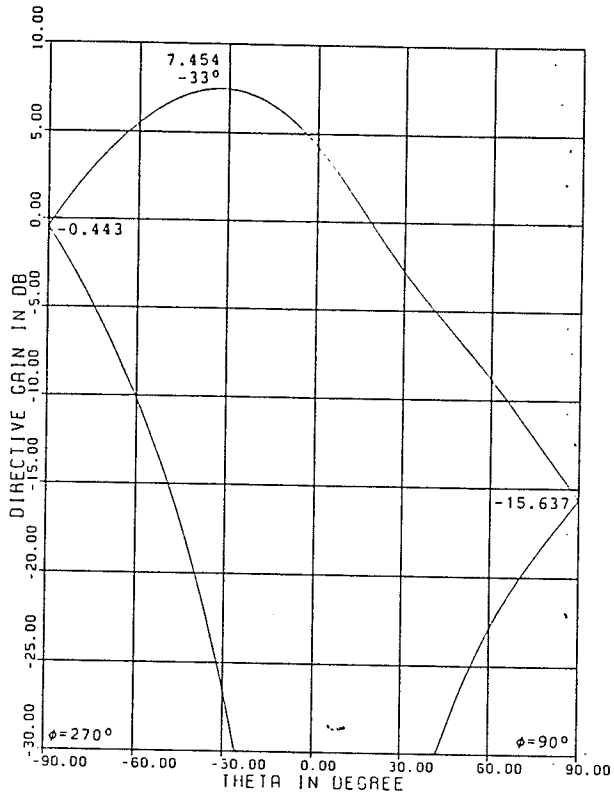

(b) H=0.1λ, $V_{11}=V_{21}=1.0$

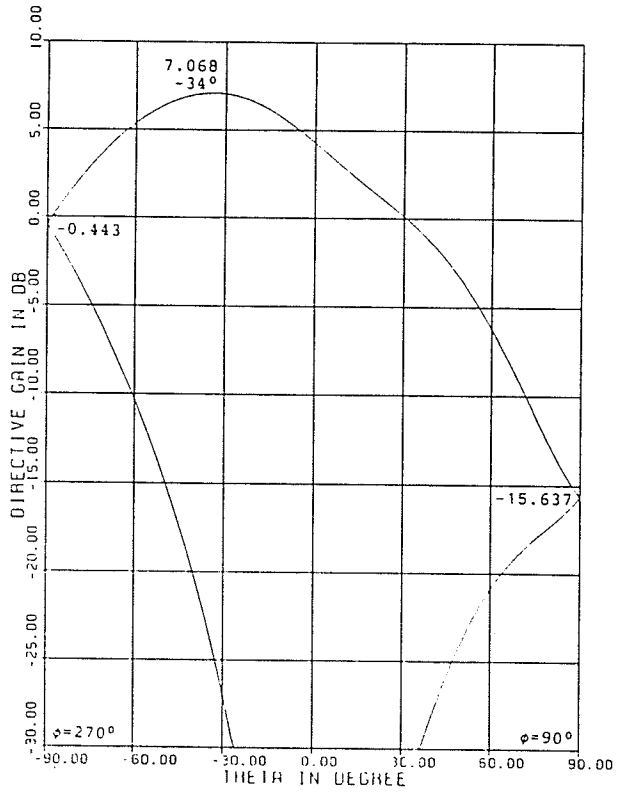

(c) H=0.15λ, $V_{11}=V_{21}=1.0$

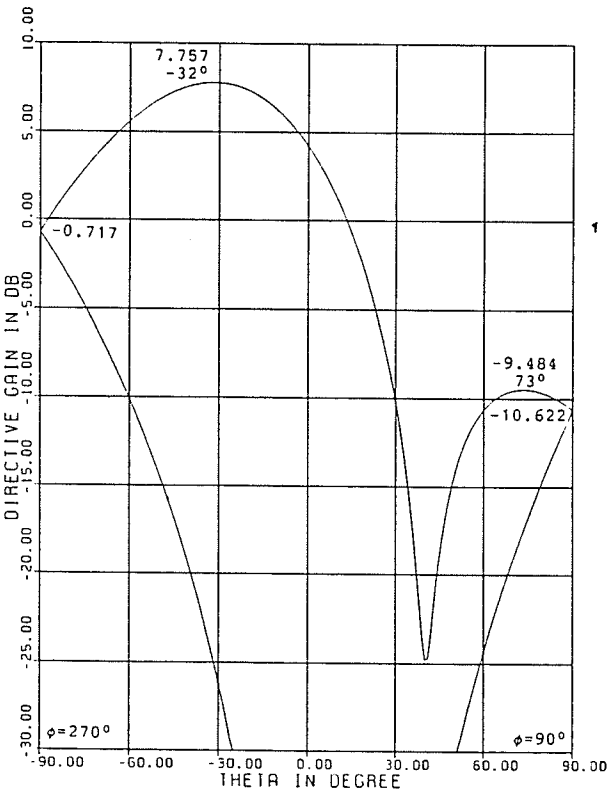

(d) h=0.1λ, $V_{11}=1.0$, $\theta_{11}=-30°$, $V_{21}=1.0$

Figure 17: Pattern of a two layer microstrip antenna with an air-gap H, $\epsilon_r=2.32$

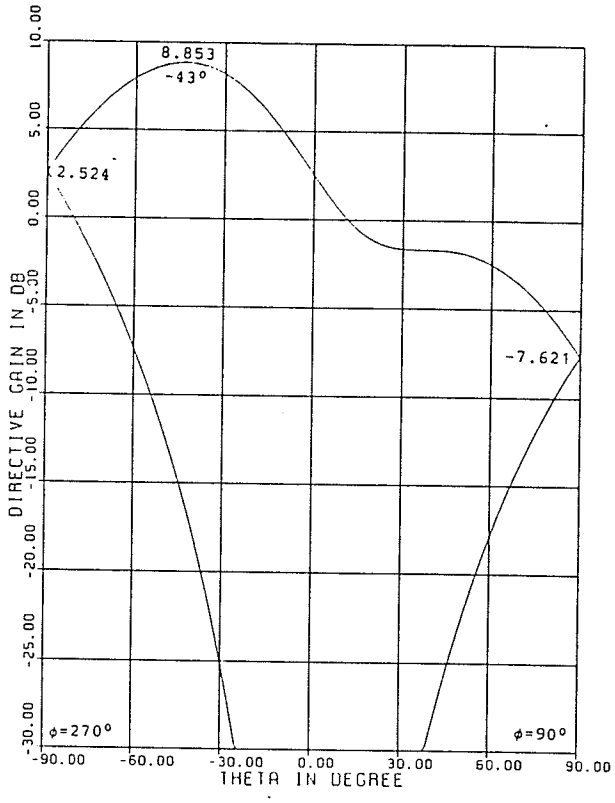

(a) $V_{11}=V_{21}=V_{31}=1.0$

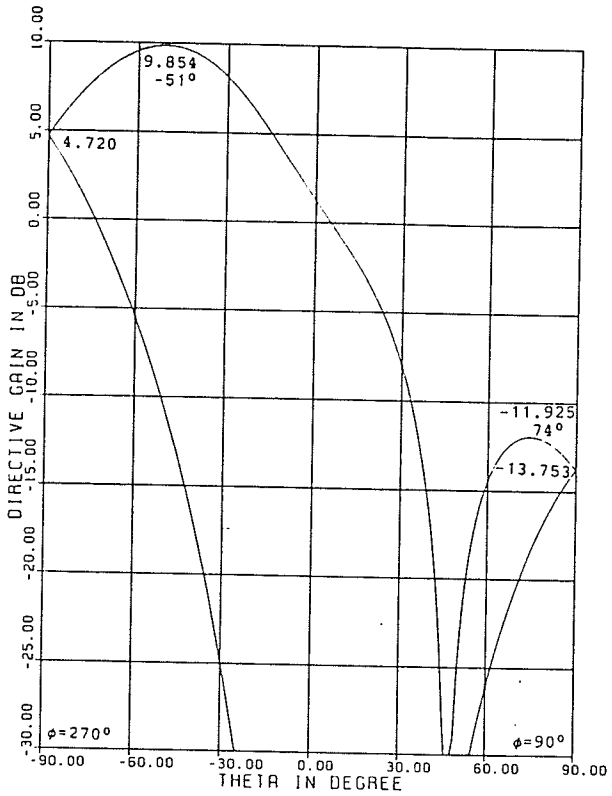

(b) $V_{11}=V_{21}=V_{31}=V_{41}=1.0$

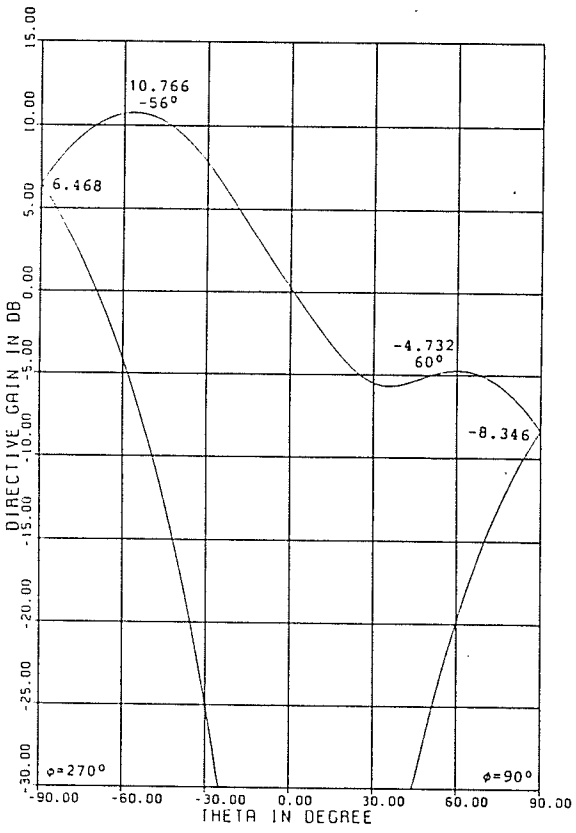

(c) $V_{11}=V_{21}=V_{31}=V_{41}=V_{51}=1.0$

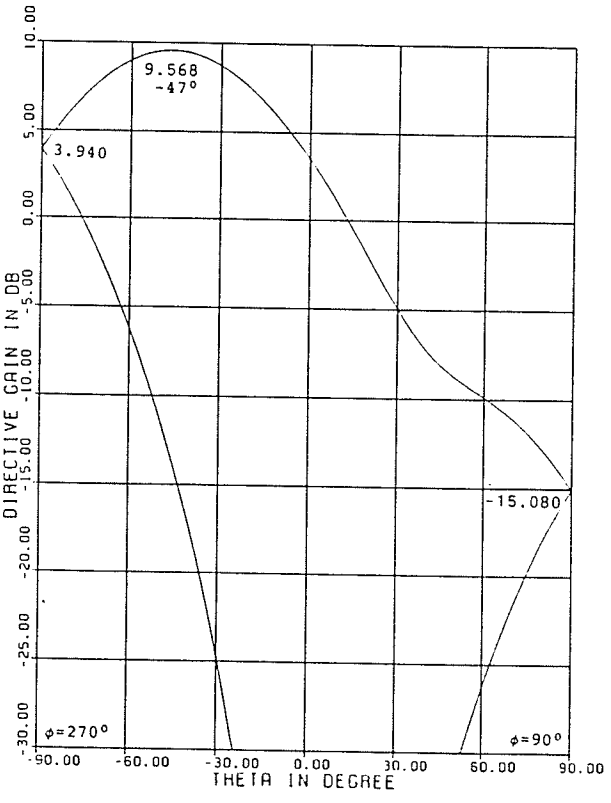

(d) $V_{11}=V_{21}=2.0$, $V_{31}=1.0$, $V_{41}=V_{51}=0.5$

Figure 18: Pattern of multiple layered microstrip structures with $\epsilon_r=2.32$

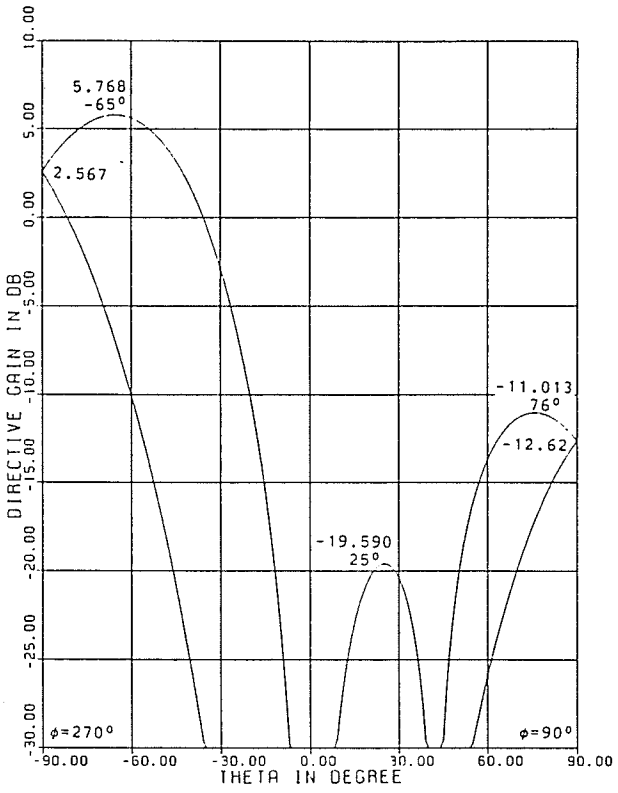

(a) Array of two, D=0.5λ

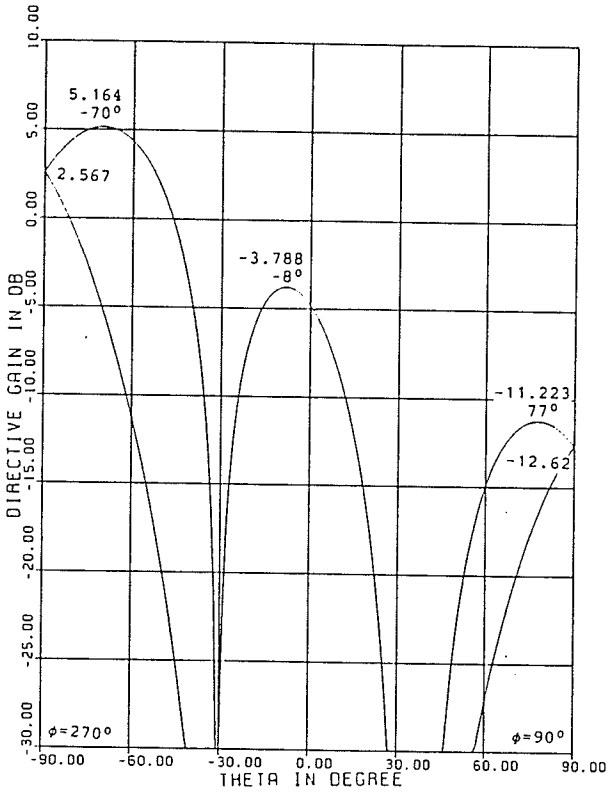

(b) Array of two, D=0.58λ

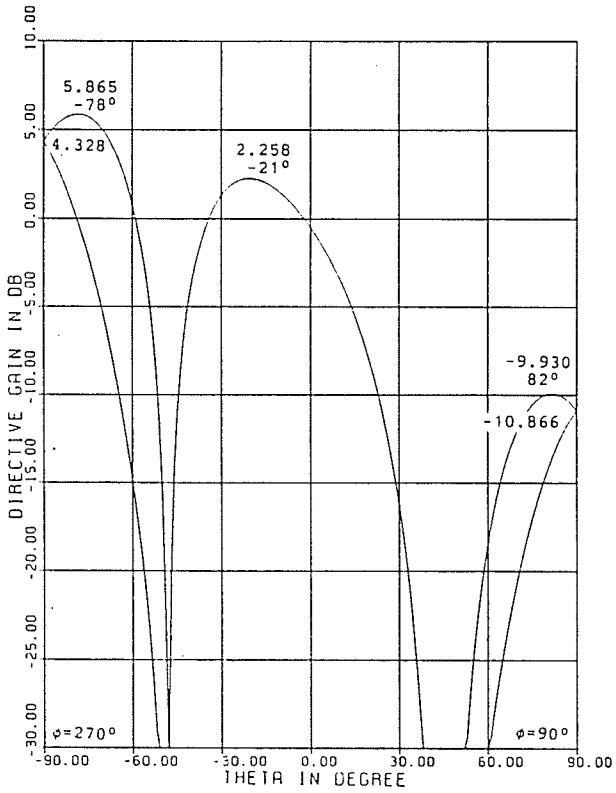

(c) Array of three, D=0.5λ

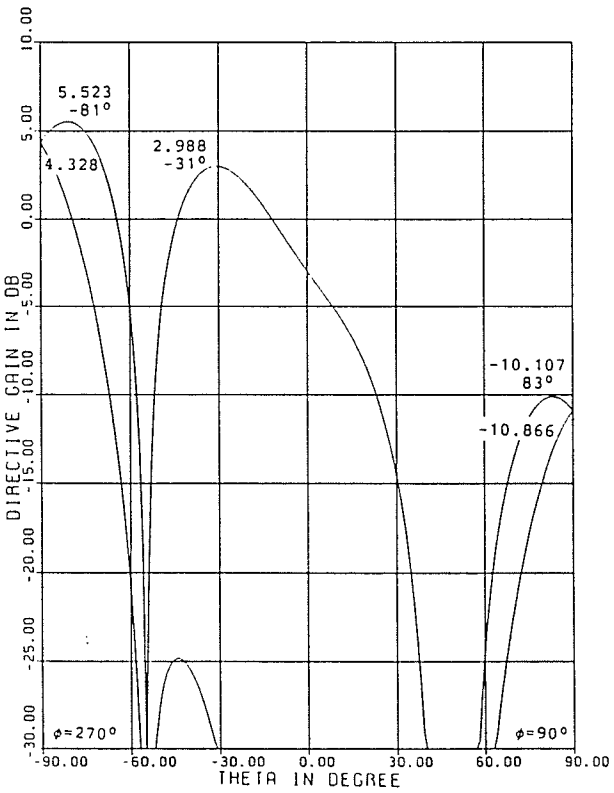

(d) Array of three, D=0.58λ

Figure 19: Pattern of a linear vertical array of two layer stacked microstrip antenna fed by unity voltage, $\epsilon_r = 2.32$

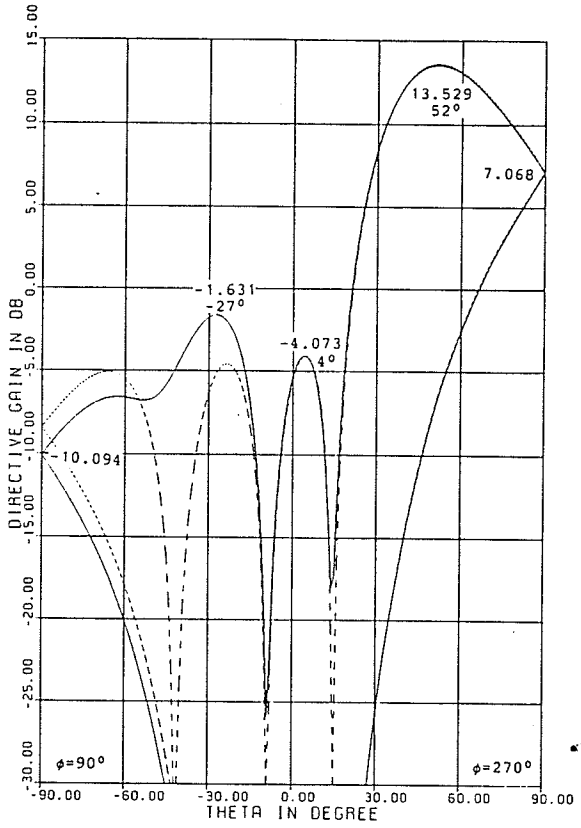

(a) $\phi_0=270^0$, $V_{11}=V_{21}=1.0$, $D=0.65\lambda$

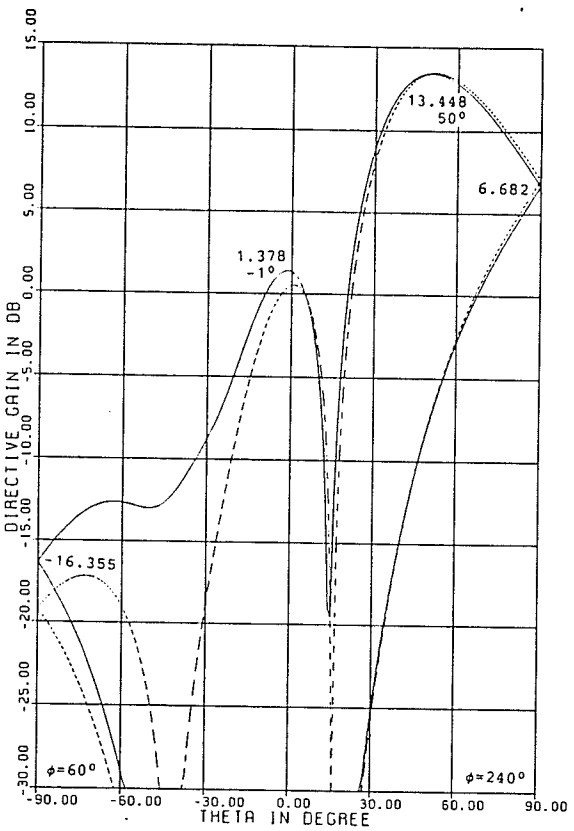

(b) $\phi_0=240^0$, $V_{11}=V_{21}=1.0$, $\theta_{21}=30^0$, $D=0.65\lambda$

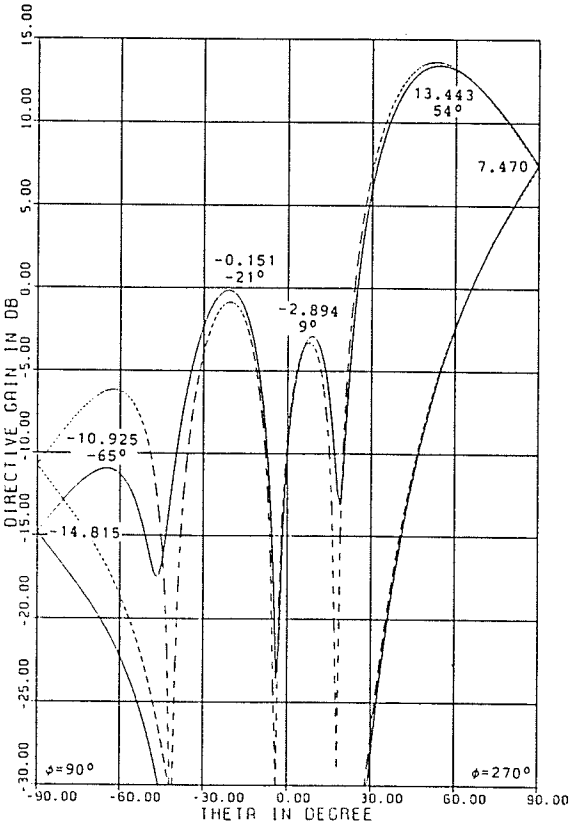

(c) $\phi_0=270^0$, $V_{11}=V_{21}=1.0$, $D=0.70\lambda$

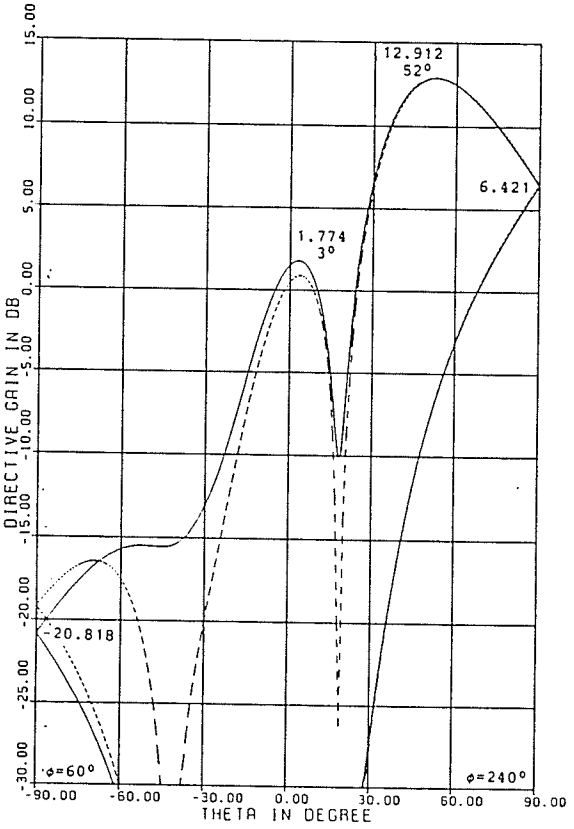

(d) $\phi_0=240^0$, $V_{11}=V_{21}=1.0$, $\theta_{21}=30^0$, $D=0.70\lambda$

Figure 20: A planar array of seven two layer stacked microstrip antenna in hexagonal shape at $\theta_0=70^0$
—— coupling, --- no coupling

Chapter VI

CONCLUSIONS

It was the objective of this thesis to present a study on the mutual coupling of a microstrip antenna array. For a practical purpose, voltage source was used, instead of the conventionally adopted current source, for patch excitation. The effective voltages, responsible for radiation, and the active input impedance of the array elements were derived in terms of the self and mutual admittance, the applied voltages, and the source internal resistance and were established in matrix formulations.

A magnetic current model was used to determine the reaction between two microstrip patches. Applying the reaction concept, the mutual admittance could be obtained. It was shown that the E-plane coupling was stronger than its H-plane counterpart. By writing $x_i=y_i=0$ in the mutual admittance expression, the self conductance could also be found with a removable singularity. Modelling the microstrip as a resonator, the self susceptance could be determined after the information of the total stored energy under the patch with an extended radius was known.

The pattern formulations were derived in terms of the vector potentials where both magnetic and electric currents

were assumed on the radiating aperture. A basic array factor was used to produce the array pattern. In both linear and circular polarizations, the gain pattern was obtained by using the total radiated power of the array as the normalization factor. A hexagonal array of seven circular microstrip was studied which gave good circular polarization pattern. It was found that the lower the substrate permittivity, the higher the co-polar component, and the more the pattern deformation due to the coupling. The cross polarization component varied directly with the phase excitation θ_0 but indirectly with the element spacing, and the permittivity of the substrate, in general. The bandwidth of the microstrip antenna could be enlarged by either decreasing the substrate permittivity or increasing its thickness.

Finally, multi-layer stacked microstrip antenna was studied. The characteristics and operations of a two-stacked microstrip were discussed. It was designed to respond to a particular frequency with a combination of different resonant modes in the radiation zone. The radiation pattern could be adjusted by the number of stacked elements and their feed voltages. It was found that the stacked microstrip gave higher gain but the pattern varied excessively with the azimuthal ϕ-angle. It could be generalized to multi-layer stacked microstrip antennas and arrays.

Appendix A

FEED LOCATION AND SELF WALL ADMITTANCE

In many antenna systems, a minimum power reflection means a maximum power transmission. It is essential to have the input impedance of the microstrip antenna matched with the internal resistance of its source in order to minimize the reflected power. This may be controlled by choosing a feed position on the patch properly and can be described by the following expression [23].

$$\frac{\pi a}{h}\cdot\left[\frac{J_n(k_{nm}a)}{J_n(k_{nm}c)}\right]^2 Y_{ii}^{w}\cdot R_i = 1 \qquad (A1)$$

where $J_n(X)$ is the Bessel function of order n, Y_{ii}^{w} is the wall admittance of the patch, R_i is the internal resistance of the source, h is the substrate thickness, c is the feed point with respect to the patch center and a is the radius of the patch. Numerical data are collected in the following tables where the normalized feed locations along with the patch dimensions and its self wall admittance are listed. They are obtained at a resonant frequency of 0.832GHz and a substrate thickness of 0.00441λ with the dielectric constant as a parameter. It is found that a higher operating mode or a lower dielectric constant material requires a larger disc radius and forces the feed matching position away from the center.

Mode	Radius (λ)	Feed (c/a)	Self Wall Admittance (mho)
TM_{11}	0.28381	0.247	0.1356E-04+j0.1069E-03
TM_{21}	0.47611	0.477	0.1140E-04+j0.9282E-04
TM_{31}	0.65818	0.593	0.9745E-05+j0.8308E-04
TM_{41}	0.83552	0.663	0.8530E-05+j0.7582E-04
TM_{51}	1.01000	0.709	0.7561E-05+j0.7025E-04
TM_{61}	1.18260	0.742	0.6747E-05+j0.6573E-04

TABLE 3

Feed positions for impedance matching with ϵ_r=1.0

Mode	Radius (λ)	Feed (c/a)	Self Wall Admittance (mho)
TM_{11}	0.25958	0.242	0.1434E-04+j0.1103E-03
TM_{21}	0.43519	0.466	0.1164E-04+j0.9556E-04
TM_{31}	0.60144	0.579	0.9691E-05+j0.8541E-04
TM_{41}	0.76335	0.647	0.8259E-05+j0.7797E-04
TM_{51}	0.92266	0.692	0.7128E-05+j0.7214E-04
TM_{61}	1.08020	0.724	0.6226E-05+j0.6748E-04

TABLE 4

Feed positions for impedance matching with ϵ_r=1.2

Mode	Radius (λ)	Feed (c/a)	Self Wall Admittance (mho)
TM_{11}	0.23262	0.236	0.1528E-04+j0.1156E-03
TM_{21}	0.38975	0.452	0.1177E-04+j0.9998E-04
TM_{31}	0.53850	0.559	0.9291E-05+j0.8911E-04
TM_{41}	0.68334	0.622	0.7454E-05+j0.8123E-04
TM_{51}	0.82585	0.663	0.6055E-05+j0.7508E-04
TM_{61}	0.96678	0.691	0.4924E-05+j0.7017E-04

TABLE 5

Feed positions for impedance matching with ϵ_r=1.5

Mode	Radius (λ)	Feed (c/a)	Self Wall Admittance (mho)
TM_{11}	0.18751	0.218	0.1628E-04+j0.1314E-03
TM_{21}	0.31395	0.408	0.1038E-04+j0.1125E-03
TM_{31}	0.43360	0.500	0.6634E-05+j0.9996E-04
TM_{41}	0.55010	0.545	0.4235E-05+j0.9084E-04
TM_{51}	0.66472	0.574	0.2695E-05+j0.8375E-04
TM_{61}	0.77807	0.593	0.1735E-05+j0.7812E-04

TABLE 6

Feed positions for impedance matching with ϵ_r=2.32

Appendix B

NUMERICAL DATA ON ACTIVE INPUT IMPEDANCE

The active input impedance of a seven element microstrip array, as shown in Fig. 8, are computed and tabulated in the following tables. Fed individually for circular polarization, each element is operated at 0.832GHz (TM_{11} mode) with ϵ_r=2.32 and the array is arranged to beam at ϕ=30°. Initially, each patch is designed to match a 50Ω cable. Table 7 to 9 showing to certain extent that how active input impedance of the array are affected by the closeness of its elements and the excitation phase through scanning.

Element	Z(Ω), θ_0=0°	Z(Ω), θ_0=60°
1	39.36 + j22.360	43.13 + j11.490
2	39.35 + j22.360	43.13 + j11.490
3	39.37 + j22.360	46.37 + j15.890
4	39.36 + j22.360	49.53 + j29.510
5	39.35 + j22.370	49.52 + j29.540
6	39.35 + j22.360	46.36 + j15.900
7	23.55 + j5.5590	38.84 + j33.910

TABLE 7

Active input impedance with element spacing at 0.40λ

Element	$Z(\Omega)$, $\theta_0=0^\circ$	$Z(\Omega)$, $\theta_0=60^\circ$
1	49.41 - j3.443	50.23 - j3.290
2	49.41 - j3.443	50.23 - j3.290
3	49.41 - j3.439	49.87 - j3.089
4	49.41 - j3.439	49.78 - j2.691
5	49.42 - j3.443	49.78 - j2.693
6	49.41 - j3.444	49.87 - j3.091
7	46.12 - j5.550	50.13 - j4.694

TABLE 8

Active input impedance with element spacing at 0.55λ

Element	$Z(\Omega)$, $\theta_0=0^\circ$	$Z(\Omega)$, $\theta_0=60^\circ$
1	49.40 + j0.9124	49.22 + j0.7772
2	49.40 + j0.9124	49.22 + j0.7772
3	49.41 + j0.9114	49.28 + j0.7976
4	49.40 + j0.9113	49.22 + j0.8318
5	49.40 + j0.9117	49.22 + j0.8314
6	49.40 + j0.9122	49.28 + j0.7979
7	48.94 + j1.4690	48.18 + j1.0910

TABLE 9

Active input impedance with element spacing at 0.70λ

Appendix C

VECTOR POTENTIALS

If $\bar{K}(r')$ and $\bar{M}(r')$ are the electric and magnetic current sources, respectively, the magnetic and electric vector potentials observed from a distant point are given by

$$\bar{A} = \frac{\mu}{4\pi} \iint_s \bar{K}(r') \frac{e^{-jk_o|\bar{r}-\bar{r}'|}}{|\bar{r}-\bar{r}'|} ds' \qquad (C1)$$

$$\bar{F} = \frac{\epsilon}{4\pi} \iint_s \bar{M}(r') \frac{e^{-jk_o|\bar{r}-\bar{r}'|}}{|\bar{r}-\bar{r}'|} ds' \qquad (C2)$$

where μ and ϵ are the permeability and permittivity of the medium, respectively. Consider a current source in a circular configuration as shown in Fig. 21, the position vectors

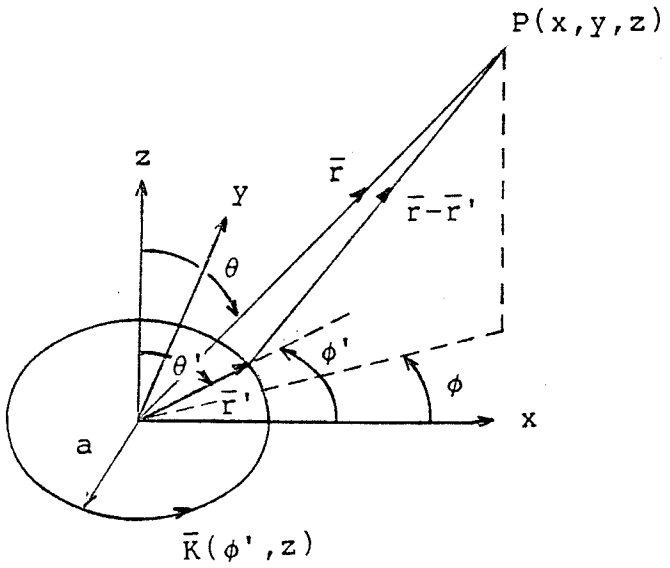

Figure 21: Far field notation for a current source

with respect to an observation point P can be expressed as

$$\bar{r} = \bar{x}\, r\sin\theta\cos\phi + \bar{y}\, r\sin\theta\sin\phi + \bar{z}\, r\cos\theta \qquad (C3)$$

$$\bar{r}' = \bar{x}\, r'\sin\theta'\cos\phi' + \bar{y}\, r'\sin\theta'\sin\phi' + \bar{z}\, r'\cos\theta' \qquad (C4)$$

If the source is an electric current sheet which extends from the x-y plane to z=h and having a as its radius, then $\bar{K}(r')=\bar{K}(\phi',z)$, $\theta'=\pi/2$, $r'=a$, $ds'=ad\phi dz$ and

$$|\bar{r}-\bar{r}'| = [\, r^2-a^2-2ra\sin\theta\cos(\phi'-\phi)\,] \qquad (C5)$$

In the far field region where $r \gg r'$ (i.e. $r \gg a$), $|\bar{r}-\bar{r}'|$ in the denominator of equation C1 can be approximated by r but $|\bar{r}-\bar{r}'|$ in the phase expression is expanded in binomial expansion and truncated to the first two terms which then becomes

$$|\bar{r}-\bar{r}'| = r-a\sin\theta\cos(\phi'-\phi) \qquad (C6)$$

The magnetic vector potential can thus be expressed as

$$\bar{A} = \frac{\mu}{4\pi r} e^{-jk_0 r} \int_0^h \int_0^{2\pi} \bar{K}(\phi',z)\, e^{jk_0 a\sin\theta\cos(\phi'-\phi)}\, ad\phi dz \qquad (C7)$$

Similarly, the electric vector potential can be determined and written in the same form as

$$\bar{F} = \frac{\epsilon}{4\pi r} e^{-jk_0 r} \int_0^h \int_0^{2\pi} \bar{M}(\phi',z)\, e^{jk_0 a\sin\theta\cos(\phi'-\phi)}\, ad\phi dz \qquad (C8)$$

Appendix D

NUMERICAL RESULTS ON RETURN LOSS AND BANDWIDTH

Failed to operate the microstrip patch at its resonant frequency would severely affect its input impedance, responsible for matching, and experience with a high return loss and low power gain performance. A single microstrip patch is studied under different operating frequencies. The power gain, input impedance, and the calculated return loss of the first three operating modes of a single circular patch are tabulated, as shown in Table 10 to 21, for each different normalized operating frequency with the substrate permittivity and its thickness as parameters. The resonant frequency is 0.832GHz and the resonant impedance is designed at 50Ω. Return loss of -6.02dB and -9.54dB correspond to reflection coefficients of 1/2 and 1/3, respectively. It is apparent that the bandwidth is much narrower for the higher ordered mode than that of the lower one. It is also found that the bandwidth of a microstrip antenna can be increased by using a substrate of lower dielectric constant or by increasing the substrate thickness.

f/f_o	Gain (dB)	Input impedance (Ω)	Return loss (dB)
0.99800	5.647	18.37 + j24.03	-6.69
0.99870	6.258	25.12 + j24.92	-9.63
0.99860	6.373	26.91 + j24.85	-10.44
1.00000	7.251	50.00	-
1.00140	6.437	26.85 - j25.01	-10.42
1.00150	6.326	25.12 - j25.08	-9.59
1.00200	5.694	17.92 - j24.05	-6.52

TABLE 10

Return loss of a disc at TM_{11} mode, ϵ_r=2.32, h=0.00441λ

f/f_o	Gain (dB)	Input impedance (Ω)	Return loss (dB)
0.99900	2.789	17.31 + j23.75	-6.27
0.99930	3.522	25.19 + j24.96	-9.62
0.99950	4.005	34.06 + j23.26	-14.44
1.00000	4.500	50.00	-
1.00050	4.058	34.62 - j23.11	-14.81
1.00070	3.649	26.44 - j25.00	-10.23
1.00100	2.813	16.99 - j23.72	-6.15

TABLE 11

Return loss of a disc at TM_{21} mode, ϵ_r=2.32, h=0.00441λ

f/f_0	Gain (dB)	Input impedance (Ω)	Return loss (dB)
0.99947	2.597	18.09 + j24.01	-6.58
0.99963	3.355	27.06 + j24.90	-10.52
0.99970	3.630	32.20 + j23.92	-13.29
1.00000	4.204	50.00	-
1.00030	3.594	30.95 - j24.30	-12.57
1.00037	3.315	25.98 - j25.00	-10.00
1.00053	2.554	17.38 - j23.83	-6.30

TABLE 12

Return loss of a disc at TM_{31} mode, ϵ_r=2.32, h=0.00441λ

f/f_0	Gain (dB)	Input impedance (Ω)	Return loss (dB)
0.99750	8.242	18.34 + j24.00	-6.68
0.99800	8.751	23.71 + j24.87	-8.95
0.99820	8.938	26.33 + j24.87	-10.17
1.00000	9.862	50.00	-
1.00180	9.031	26.42 - j25.05	-10.21
1.00200	8.852	23.76 - j25.06	-8.98
1.00250	8.362	18.31 - j24.18	-6.67

TABLE 13

Return loss of a disc at TM_{11} mode, ϵ_r=1.0, h=0.00441λ

f/f_0	Gain (dB)	Input impedance (Ω)	Return loss (dB)
0.99830	5.300	16.88 + j23.58	-6.10
0.99880	6.101	25.33 + j24.94	-9.69
0.99900	6.377	29.86 + j24.46	-11.97
1.00000	7.080	50.00	-
1.00100	6.399	29.25 - j24.70	-11.64
1.00110	6.269	26.95 - j24.98	-10.47
1.00180	5.172	15.25 - j23.08	-5.47

TABLE 14

Return loss of a disc at TM_{21} mode, ϵ_r=1.0, h=0.00441λ

f/f_0	Gain (dB)	Input impedance (Ω)	Return loss (dB)
0.99880	5.190	17.54 + j23.82	-6.36
0.99920	6.045	27.50 + j24.83	-10.74
0.99940	6.389	34.30 + j23.16	-14.60
1.00000	6.878	50.00	-
1.00060	6.404	33.76 - j23.46	-14.25
1.00080	6.065	27.00 - j24.96	-10.49
1.00120	5.223	17.21 - j23.80	-6.23

TABLE 15

Return loss of a disc at TM_{31} mode, ϵ_r=1.0, h=0.00441λ

f/f_0	Gain (dB)	Input impedance (Ω)	Return loss (dB)
0.99000	4.816	16.10 + j23.02	-5.79
0.99350	5.858	26.26 + j24.62	-10.14
0.99600	6.442	37.10 + j21.54	-16.58
1.00000	6.901	50.00	-
1.00400	6.642	37.30 - j22.10	-16.74
1.00650	6.165	26.13 - j25.31	-10.07
1.01000	5.246	15.64 - j23.52	-5.62

TABLE 16

Return loss of a disc at TM_{11} mode, ϵ_r=2.32, h=0.02205λ

f/f_0	Gain (dB)	Input impedance (Ω)	Return loss (dB)
0.99550	2.115	16.61 + j23.39	-5.99
0.99600	2.443	19.28 + j24.18	-7.06
0.99700	3.046	26.27 + j24.81	-10.14
1.00000	4.021	50.00	-
1.00300	3.242	26.51 - j25.11	-10.25
1.00400	2.691	19.33 - j24.51	-7.08
1.00450	2.386	16.58 - j23.70	-5.98

TABLE 17

Return loss of a disc at TM_{21} mode, ϵ_r=2.32, h=0.02205λ

f/f_0	Gain (dB)	Input impedance (Ω)	Return loss (dB)
0.99770	2.107	17.64 + j23.81	-6.40
0.99830	2.798	24.97 + j24.92	-9.52
0.99850	3.003	28.08 + j24.72	-11.04
1.00000	3.833	50.00	-
1.00150	3.099	27.81 - j24.93	-10.89
1.00170	2.905	24.69 - j25.08	-9.40
1.00230	2.249	17.38 - j23.90	-6.30

TABLE 18

Return loss of a disc at TM_{31} mode, ϵ_r=2.32, h=0.02205λ

f/f_0	Gain (dB)	Input impedance (Ω)	Return loss (dB)
0.98800	7.320	18.05 + j23.56	-6.56
0.99200	8.220	27.75 + j24.40	-10.86
0.99500	8.754	37.88 + j20.98	-17.21
1.00000	9.209	50.00	-
1.00500	9.006	38.22 - j21.67	-17.49
1.00800	8.604	27.67 - j25.30	-10.82
1.01200	7.850	17.54 - j24.30	-6.36

TABLE 19

Return loss of a disc at TM_{11} mode, ϵ_r=1.0, h=0.02205λ

f/f_0	Gain (dB)	Input impedance (Ω)	Return loss (dB)
0.99200	4.470	16.54 + j23.24	-5.97
0.99450	5.379	25.44 + j24.72	-9.74
0.99500	5.540	27.78 + j24.56	-10.88
1.00000	6.467	50.00	-
1.00400	6.047	32.96 - j23.98	-13.74
1.00500	5.800	27.60 - j25.14	-10.79
1.00550	5.661	25.20 - j25.28	-9.63

TABLE 20

Return loss of a disc at TM_{21} mode, ϵ_r=1.0, h=0.02205λ

f/f_0	Gain (dB)	Input impedance (Ω)	Return loss (dB)
0.99400	4.176	15.80 + j23.04	-5.68
0.99500	4.696	19.93 + j24.28	-7.33
0.99600	5.175	25.39 + j24.79	-9.72
1.00000	6.236	50.00	-
1.00300	5.762	32.23 - j24.13	-13.31
1.00400	5.396	25.20 - j25.20	-9.63
1.00500	4.965	19.65 - j24.62	-7.22

TABLE 21

Return loss of a disc at TM_{31} mode, ϵ_r=1.0, h=0.02205λ

REFERENCES

1. Munson R.E., "Conformal Microstrip Antennas and Microstrip Phased Arrays", IEEE Trans. Antennas Propagat., Vol. AP-22, No. 1, Jan. 1974, pp. 74-78.

2. Howell J.Q., "Microstrip Antennas", IEEE Trans. Antennas Propagat., Vol. AP-23, No. 1, Jan. 1975, pp. 90-93.

3. Derneryd A.G., "Linearly Polarized Microstrip Antennas", IEEE Trans. Antennas Propagat., Vol. AP-24, No. 6, Nov. 1976, pp. 846-851.

4. Garvin C.W., Munson R.E., Ostwald L.T., and Schroeder K.G., "Missile Base Mounted Microstrip Antennas", IEEE Trans. Antennas Propagat., Vol. AP-25, Sept. 1977, pp. 604-610.

5. Shen L.C., Long S.A., Allerding M.R., and Walton M.D., "Resonant Frequency of a Circular Disc, Printed Circuit Antenna", IEEE Trans. Antennas Propagat., Vol. AP-25, No. 5, Jul. 1977, pp. 595-596.

6. Agrawal P.K. and Bailey M.C., "An Analysis Technique for Microstrip Antennas", IEEE Trans. Antennas Propagat., Vol. AP-25, No. 6, Nov. 1977, pp. 756-759.

7. Watkins J., "Circular Resonant Structures in Microstrip", Electronics Letters, Vol. 5, No. 21, Oct. 1969, pp. 524-525.

8. Itoh T. and Mittra R., "Analysis of Microstrip Disk Resonator", Arch. Elek. Ubertagung, Vol. 27, Nov. 1973, pp. 456-458.

9. Wolff I. and Knoppik N., "Rectangular and Circular Microstrip Disk Capacitors and Resonators", IEEE Trans. Microwave Theory Tech., Vol. MTT-22, No. 10, Oct. 1974, pp. 857-864.

10. Long S.A., Shen L.C., Walton M.D., and Allerding M.R., "Impedance of a Circular Disc Printed Circuit Antenna", Electronics Letters, Vol. 14, No. 21, Oct. 1978, pp. 684-686.

11. Derneryd A.G., "A Theoretical Investigation of the Rectangular Microstrip Antenna Element", IEEE Trans. Antennas Propagat., Vol. AP-26, No. 4, Jul. 1978, pp. 532-535.

12. Derneryd A.G., "Analysis of the Microstrip Disk Antenna Element", IEEE Trans. Antennas Propagat., Vol. AP-27, No. 5, Sept. 1979, pp. 660-664.

13. Lo Y.T., Solomon D., Richards W.F., "Theory and Experiment on Microstrip Antennas", IEEE Trans. Antennas Propagat., Vol. AP-27, No. 2, Mar. 1979, pp. 137-145.

14. Richards W.F., Lo Y.T., Harrison D.D., "Improved Theory for Microstrip Antennas", Electronics Letters, Vol. 15, No. 2, Jan. 1979, pp. 42-44.

15. Chew W.C. and Kong J.A., "Effect of Fringing Fields on the Capacitance of Circular Microstrip Disc", IEEE Trans. Microwave Theory Tech., Vol. MTT-28, No. 2, Feb. 1980, pp. 98-104.

16. Bahl I.J. and Bhartia P., "Microstrip Antenna", Artech House, Inc., Dedham, MA 1980.

17. Harrington R.F., "Time Harmonic Electromagnetic Fields", McGraw-Hill Book Company, New York 1961.

18. Newman E.H. and Tulyathan P., "Analysis of Microstrip Antennas Using Moment Methods", IEEE Trans. Antennas Propagat., Vol. AP-29, No. 1, Jan. 1981, pp. 47-53.

19. Bhattacharyya A.K., "Generalized Transmission Line Model of Microstrip Patch Antennas and Some Applications", Ph.D. Thesis, Indian Institute of Technology, Kharagpur-721 302, India, Feb. 1985.

20. Ma M.T., "Theory and Application of Antenna Arrays", Wiley-Interscience Publication, John Wiley & Sons, Inc. 1974.

21. Parks F.G. and Bailey M.C., "Mutual Coupling Between Microstrip Disk Antennas", in Dig. Int. Symp. Antennas Propagat. Soc., Amherst, MA Oct. 1976, pp. 399-402.

22. Jedlicka R.P., Poe M.T., and Carver K.R., "Measured Mutual Coupling Between Microstrip Antennas", IEEE Trans. Antennas Propagat., Vol. AP-29, No. 1, Jan. 1981, pp. 148-150.

23. Bhattacharyya A.K., Shafai L. et al., "Performance of Planar Microstrip Arrays Including Mutual Coupling", MSAT application, Department of Electrical Engineering, University of Manitoba, Jan. 1987.

24. Bhattacharyya A.K. and Garg R., "Self and Mutual Admittance between Two Concentric, Coplanar, Circular Radiating Current Sources", IEE Proceedings, Vol. 131, Pt. H, No. 3, June 1984, pp. 217-219.

25. Yano S. and Ishimaru A., "A Theoretical Study of the Input Impedance of a Circular Microstrip Disk Antenna", IEEE Trans. Antennas Propagat., Vol. AP-29, No. 1,Jan. 1981, pp. 77-83.

26. James J.R., Hall P.S, and Wood C., "Microstrip Antenna Theory and Design", Peter Peregrinus Ltd., IEE, London and New York 1981.

27. Chen C.H., Tulintseff A., and Sorbello R.M., "Broadband Two-Layer Microstrip Antenna", IEEE AP-S Int. Symp. Digest 1984, pp. 250-254.

28. Wang B.F. and Lo Y.T., "Microstrip Antenna for Dual-Frequency Operation", IEEE AP-S Int. Symp. Digest 1984, pp. 551-554.